The Evolution of Supermassive Population III Stars

Lionel Haemmerlé[1*], T. E. Woods[2], Ralf S. Klessen[1,4], Alexander Heger[2], Daniel J. Whalen[3]

[1] *Universität Heidelberg, Zentrum für Astronomie, Institut für Theoretische Astrophysik, Albert-Ueberle-Str. 2, D-69120 Heidelberg, Germany*
[2] *Monash Centre for Astrophysics, School of Physics and Astronomy, Monash University, VIC 3800, Australia*
[3] *Institute of Cosmology and Gravitation, University of Portsmouth, Dennis Sciama Building, Portsmouth PO1 3FX, UK*
[4] *Interdisziplinäres Zentrum für wissenschaftliches Rechnen der Universität Heidelberg, Im Neuenheimer Feld 205, D-69120 Heidelberg, Germany*

ABSTRACT

Supermassive primordial stars forming in atomically-cooled halos at $z \sim 15-20$ are currently thought to be the progenitors of the earliest quasars in the Universe. In this picture, the star evolves under accretion rates of $0.1 - 1$ $M_\odot \, yr^{-1}$ until the general relativistic instability triggers its collapse to a black hole at masses of $\sim 10^5$ $M_\odot$. However, the ability of the accretion flow to sustain such high rates depends crucially on the photospheric properties of the accreting star, because its ionising radiation could reduce or even halt accretion. Here we present new models of supermassive Population III protostars accreting at rates $0.001 - 10$ $M_\odot \, yr^{-1}$, computed with the GENEVA stellar evolution code including general relativistic corrections to the internal structure. We compute for the first time evolutionary tracks in the mass range $M > 10^5 \, M_\odot$. We use the polytropic stability criterion to estimate the mass at which the collapse occurs, which has been shown to give a lower limit of the actual mass at collapse in recent hydrodynamic simulations. **We find that at accretion rates higher than 0.01 $M_\odot \, yr^{-1}$ the stars evolve asymptotically as red, cool supergiants with surface temperatures below 10^4 K towards masses $> 10^5$ $M_\odot$. Moreover, even with the lower rates 0.001 $M_\odot yr^{-1} < \dot{M} < 0.01$ $M_\odot \, yr^{-1}$, the surface temperature is substantially reduced from 10^5 K to 10^4 K for $M \gtrsim 600$ $M_\odot$.** Compared to previous studies, our results extend the range of masses and accretion rates at which the ionising feedback remains weak, reinforcing the case for direct collapse as the origin of the first quasars. We provide numerical tables for the surface properties of our models.

Key words: quasars: supermassive black holes - early universe - dark ages, reionization, first stars - stars: Population III - galaxies: high-redshift – stars: massive

1 INTRODUCTION

The properties and evolution of supermassive stars (SMS), with masses $\gtrsim 10^4$ $M_\odot$, have been studied since the early 1960s (e.g., Osaki 1966; Unno 1971; Appenzeller & Fricke 1972a,b; Fricke 1973; Shapiro & Teukolsky 1979; Fuller et al. 1986). But the existence of such stars has only recently been suspected to be necessary to explain the formation of quasars by $z \gtrsim 7$, such as ULAS J1120+0641, a 2×10^9 $M_\odot$ black hole at $z = 7.1$ (Mortlock et al. 2011) and SDSS J010013.02+280225.8, a 1.2×10^{10} $M_\odot$ black hole at $z = 6.3$ (Wu et al. 2015; see Smidt et al. 2017). The origin of these supermassive black holes (SMBHs) may not

have been $10-500$ $M_\odot$ Population III (Pop III) star BHs at $z \sim 20-25$ because they might not have achieved the rapid, sustained growth needed to exceed 10^9 $M_\odot$ by $z \gtrsim 7$ (Whalen et al. 2004; Alvarez et al. 2009; Park & Ricotti 2011; Whalen & Fryer 2012). Supercritical accretion by Pop III star BHs could allow them to grow to such masses at early times even with limited duty cycles (Volonteri et al. 2015; Inayoshi et al. 2016; Sakurai et al. 2016; Pezzulli et al. 2016), but it is not known if such processes operate in primordial accretion discs or for the times required to produce massive seeds. The seeds of the first quasars may instead have been 10^4-10^5 $M_\odot$ BHs that formed via direct collapse.

In this picture, a primordial halo forms in close proximity to nearby star-forming regions with strong Lyman-Werner (11.18 – 13.6 eV) UV and H^- photodetachment

* E-mail: Lionel.Haemmerle@unige.ch

(> 0.755 eV) fluxes that sterilise the halo by effectively destroying the main coolant, molecular hydrogen H_2 (Agarwal et al. 2012; Dijkstra et al. 2014; Agarwal et al. 2016; but see also Inayoshi & Omukai 2012; Inayoshi et al. 2015). Due to the absence of H_2 molecules, the gas temperature rises to 10^4 K, preventing fragmentation and star formation before the halo's mass reaches a few 10^7 $M_\odot$. At such masses, the halo gas finally becomes gravitationally unstable and begins to contract towards the centre with very high accretion rates of $0.1 - 10$ $M_\odot \, yr^{-1}$, forming a $10^4 - 10^5$ $M_\odot$ star in less than the lifetime of the star on the main sequence (e.g. Latif et al. 2013a,b; Becerra et al. 2015). The dynamics of these flows on the smallest scales are not yet fully understood, but in the simulations performed to date a massive line-cooled disc forms that rapidly feeds the growth of a single object at its centre. Fragmentation, if it occurs, is minor and the clumps mostly spiral into the central object (Regan et al. 2014; Inayoshi & Haiman 2014; Becerra et al. 2015). It is expected that stars in this mass range will collapse directly to BHs without exploding, with masses equal to the progenitors due to the inefficiency of radiative mass losses in metal-free stars. An observational candidate for a direct collapse black hole (DCBH) has now been found, CR7, a Ly-α emitter at $z = 6.6$ (Sobral et al. 2015; Pallottini et al. 2015; Hartwig et al. 2016; Agarwal et al. 2016). Current models favor the BH interpretation of CR7 over a Pop III starburst (Pallottini et al. 2015; Hartwig et al. 2016; Agarwal et al. 2016).

A number of studies have recently examined the evolution of supermassive Pop III protostars growing by accretion at the high rates expected for atomically-cooled haloes. Hosokawa et al. (2013) followed the growth of such objects up to $\sim 10^5$ $M_\odot$ for different constant accretion rates and found that for rates $\gtrsim 0.1$ $M_\odot \, yr^{-1}$ the protostars remain red and cool until they reach a few 10^4 $M_\odot$. Sakurai et al. (2015) studied the evolution of supermassive Pop III stars in clumpy accretion scenarios and suggest that the protostar could intermittently become blue and hot at low masses but eventually evolved onto a redder, cooler track. But the codes used in these studies did not include the general relativistic (GR) corrections to hydrostatic equilibrium, and thus the runs were stopped before the stellar mass exceeds 10^5 $M_\odot$. Indeed, above this mass, the GR effects are expected to become significant, in particular by triggering the collapse into a black hole through the GR instability (Iben 1963; Chandrasekhar 1964). Umeda et al. (2016) included the post-Newtonian corrections to their models, computing the internal structure of stars accreting at rates $0.1 - 10$ $M_\odot \, yr^{-1}$ towards masses of $1 - 8 \times 10^5$ $M_\odot$. **In their models, the collapse is triggered at these masses, due to GR instability.** However, no evolutionary tracks were displayed in this study, and the properties of the radiative feedback in their models, in particular in the highest mass-range, are not available.

In a first paper (Woods et al. 2017), we modeled the growth of supermassive Pop III stars at accretion rates of 0.01 - 10 $M_\odot \, yr^{-1}$ with the KEPLER stellar evolution code. **The KEPLER code includes a self-consistent treatment of the hydrodynamics, taking into account the post-Newtonian correction.** We found that the mass at collapse varied from $\sim 7.5 \times 10^4$ to 3.2×10^5 $M_\odot$. However, numerical difficulties in the integration of the atmosphere in case of accretion did not allow us to study the photospheric

properties of our models, and to establish the evolutionary tracks and ionising effect of the radiation field.

The actual growth rates of supermassive Pop III stars may be crucially dependent on their internal structure and surface temperature. If the star is red and cool, accretion proceeds at rates set by the cosmological flows assumed in previous evolution models. But if the star becomes compact, blue and hot its ionising radiation could reduce accretion and the final mass of the star. The accretion geometry is also critical: the ram pressure of spherical inflows at the rates previously studied would almost certainly prevent radiation from the star from ionising the flows even if it is blue and hot (Johnson et al. 2012). Accretion through a disc, which is more likely, could result in bipolar radiation breakout that disperses the flows (e.g., Hosokawa et al. 2011; Hirano et al. 2014). Clumpy accretion can likewise result in hot protostars that suppress their own growth at early times (Sakurai et al. 2015).

In the present work, we re-examine the evolution of supermassive primordial protostars accreting at high rates ($0.001 - 10$ $M_\odot \, yr^{-1}$). We present models computed with the GENEVA stellar evolution code, and describe the properties of their internal structures and evolutionary tracks. We focus on the ionising properties of the radiation field, in order to evaluate the potential of these stars to regulate their own growth. In addition, we use the polytropic criterion to study the development of the GR instability in the stellar interior, expected to trigger the collapse of the protostar into a black hole. In Sect. 2 we describe our GENEVA models. In Sect. 3 we examine their interior structure, and surface properties. In Sect. 4 we study how these surface properties depend on the treatment of their external layers, we estimate the mass at which the GR instability triggers the collapse into a black hole, and we compare our results with those of previous studies. We summarise our conclusions in Sect. 5.

2 NUMERICAL METHOD

The GENEVA code is a one-dimensional hydrostatic stellar evolution code that numerically solves the four usual equations of stellar structure (e.g. Eggenberger et al. 2008) with the Henyey method. The energy generation rate includes both nuclear reactions and gravitational contraction, opacities are derived from the OPAL tables (Iglesias & Rogers 1996), and convection is approximated by mixing-length theory. A general description of the code for the case without accretion is given in Eggenberger et al. (2008).

Accretion has recently been implemented in the GENEVA code as described in Haemmerlé et al. (2013, 2016), and we recall here only the main ideas. The accretion rate is a free parameter, fixed externally. Here we consider the following constant rates:

$$\dot{M} = 0.001, \, 0.01, \, 0.1, \, 1, \, 10 \, M_\odot \, yr^{-1} \tag{1}$$

Since the code is hydrostatic, we model only the stellar interior, without the accretion shock. Moreover, the code does not include any contribution to the luminosity from the accretion energy, and we assume that the entropy of the accreted material is the same as that of the stellar surface. This assumption corresponds to accretion onto the star through

a disc, for which any entropy excess can be efficiently radiated away in the polar direction before being advected in the stellar interior (cold disc accretion, Palla & Stahler 1992; Hosokawa et al. 2010).

GR effects are expected to be important in SMS, and to account for them we apply the first order post-Newtonian Tolman-Oppenheimer-Volkoff (TOV) correction in the equation of hydrostatic equilibrium. We replace the Newtonian gravitational constant G by

$$G_{\rm rel} = G \left(1 + \frac{P}{\rho c^2} + \frac{2GM_r}{rc^2} + \frac{4\pi P r^3}{M_r c^2} \right) \quad (2)$$

where P is the pressure, ρ the mass density, c the speed of light and M_r the mass enclosed in a radius r. This approximation to GR is the same as that in KEPLER (Fuller et al. 1986).

We emphasise that, as usual, the outer regions of the star are not included in the calculation of the stellar interior. For numerical stability, one has to neglect the production and absorption of energy in the layers with $M_r/M > {\rm fit}_M$, where ${\rm fit}_M$ is fixed externally. In these layers, the structure equations are integrated assuming a flat luminosity profile. Decreasing ${\rm fit}_M$ favours numerical convergence, while increasing it improves physical consistency. In all the models described in the present work, we fix a value of ${\rm fit}_M$ which is constant during the evolution. Depending on the models, we consider either ${\rm fit}_M = 0.999$ or ${\rm fit}_M = 0.99$. The consequences of this assumption are discussed in Sect. 4.1.

Convective zones are determined according to the Schwarzschild criterion. For numerical stability, we do not include any overshooting. The consequences of these choices are discussed in Sect. 4.3.

3 MODELS

3.1 Initial setups

Accretion at high rates onto low-mass hydrostatic cores makes numerical convergence difficult. Thus for 0.1, 1 and 10 $M_\odot$ yr^{-1} we initialise our models with a mass of $M_{\rm ini} = 10 \, M_\odot$, while for 0.01 and 0.001 $M_\odot$ yr^{-1} we take $M_{\rm ini} = 2 \, M_\odot$. The chemical composition of the initial models is homogeneous, with a hydrogen mass fraction of $X = 0.7516$, a helium mass fraction of $Y = 0.2484$, and a metallicity $Z = 1 - X - Y = 0$. We include deuterium with a mass fraction of $X_2 = 5 \times 10^{-5}$ (Bernasconi & Maeder 1996; Behrend & Maeder 2001; Haemmerlé et al. 2016). The chemical composition of the accreted material is identical to that of the initial protostellar seeds. The initial structures correspond to polytropes with $n \simeq 3/2$, with flat entropy profiles, so that the stars start their evolution as fully convective objects. The central temperatures are 4.1×10^5 K and 6.6×10^5 K for the 10 $M_\odot$ and 2 $M_\odot$ initial models, respectively, which is below the temperature required for D-burning ($T_{\rm D} \simeq 1 - 2 \times 10^6$ K). We choose the initial time-step in order to ensure that the mass accreted in the first time-step does not exceed 0.1 $M_\odot$. As a consequence, the initial time-step depends on the accretion rate, and is given by $dt = 0.1 \, M_\odot/\dot{M}$. We take ${\rm fit}_M = 0.999$ as a fiducial value, except for 0.001 $M_\odot$ yr^{-1}. The motivations and consequences of this choice are discussed in Sect. 4.1. For reasons of numerical stability, we do not include the GR correction in the model
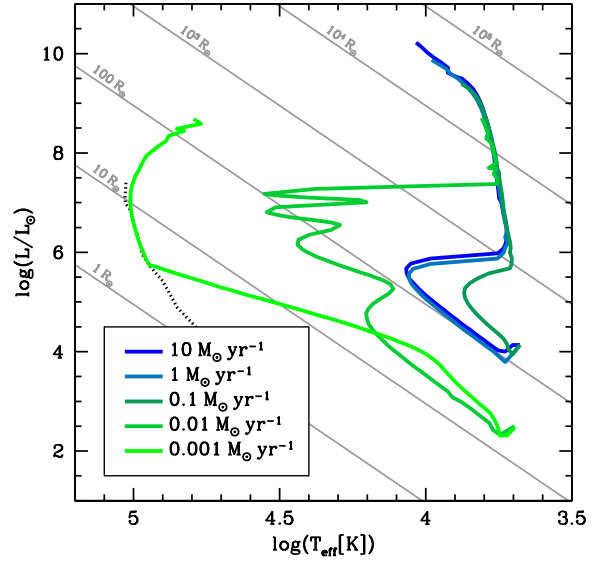

Figure 1. Evolutionary tracks on the HR diagram for the models at the indicated accretion rates. The grey straight lines indicate the stellar radius, and the black dotted curve is the ZAMS of Schaerer 2002.

at $\dot{M} = 0.001 \, M_\odot$ yr^{-1}. This model never exceeds $10^4 \, M_\odot$ significantly, so that we expect GR effects to be negligible in this case.

3.2 Evolutionary tracks and internal structures

The evolutionary tracks on the Hertzsprung-Russel (HR) diagram are shown on Fig. 1 for the five accretion rates. For all the models, the luminosity increases monotonically as the stellar mass grows by accretion, except in the very early evolution. The mass-luminosity relation is nearly independent of the accretion history (Fig. 3, lower panel). But the evolution of the effective temperature differs significantly between models at various rates. After an adjustment phase, the tracks converge towards two distinct asymptotic regimes in the HR diagram: the high-$\dot{M}$ regime ($\dot{M} \gtrsim 0.01 \, M_\odot$ yr^{-1}) gives a nearly vertical track in the red, along the Hayashi limit, while the low-$\dot{M}$ regime ($\dot{M} < 0.01 \, M_\odot$ yr^{-1}) leads to the blue, along the Zero-Age Main Sequence (ZAMS). In the high-$\dot{M}$ regime, the effective temperature is locked around 5000 – 6000 K, and thus never exceeds 10^4 K before the luminosity reaches $10^{10} \, L_\odot$. The star is bloated up, with a radius larger than 1000 $R_\odot$, as a 'red supergiant protostar' (Hosokawa et al. 2012). In the low-$\dot{M}$ regime, the track evolves immediately towards the blue, approaching $T_{\rm eff} \simeq 10^5$ K before the luminosity exceeds $10^6 \, L_\odot$. The increase in effective temperature is only stopped when the star reaches the ZAMS and stops contracting. Thus the location of the star on the HR diagram is confined between two limits: the Hayashi limit in the red and the ZAMS in the blue. Each of these limits corresponds to the asymptotic track of our models according to their accretion regime, low- or high-$\dot{M}$, i.e. depending if the rate is above or below a critical value $\dot{M}_{\rm crit} \sim 0.005 \, M_\odot$ yr^{-1}. Notice that the Hayashi limit reflects the physics at the stellar surface, while the ZAMS limit reflects the physics at the centre. Models at $\dot{M} = 0.001 \, M_\odot$ yr^{-1}
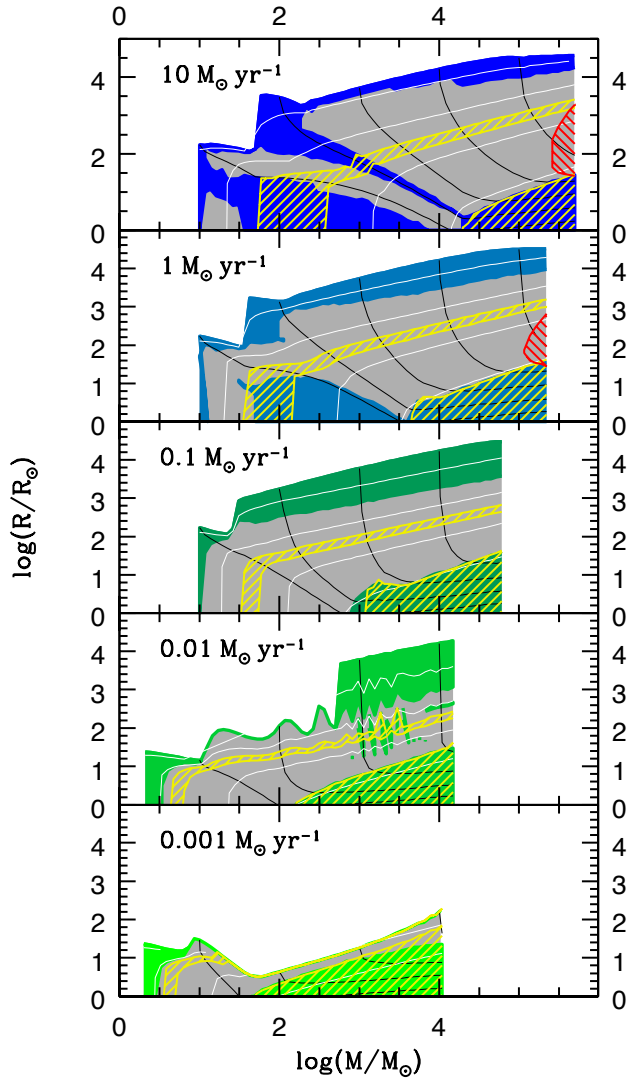
Figure 2. Internal structures of the models for the indicated accretion rates. On each panel, the upper curve is the stellar radius, the blue and green areas indicate convective zones, and the grey areas indicate radiative transport. The yellow hatched areas correspond to D- and H-burning, and the red hatched areas indicate the GR instability according to the polytropic criterion of Eq. (7) with $n = 3$. The black curves indicate the Lagrangian layers of $\log(M_r/M_\odot) = 1, 2, 3, 4$ and 5, and the white ones are isotherms of $\log(T[K]) = 5, 6, 7$ and 8.

or with $\dot{M} \geq 0.1$ M$_\odot$ yr^{-1} converge to their asymptotic track relatively early, before the luminosity exceeds significantly 10^6 L$_\odot$. For the intermediate case $\dot{M} = 0.01$ M$_\odot$ yr^{-1}, the track remains longer between the two asymptotic limits, showing oscillations in $T_{\rm eff}$ in the range $10\,000 - 30\,000$ K. Convergence towards the Hayashi limit occurs eventually when the luminosity has grown to 2×10^7 L$_\odot$.

The internal structure of these models is illustrated in Fig. 2. In addition, Fig. 3 shows the evolution of their central temperatures and surface luminosities. All five models start with a fully convective structure and a central temperature $T_c < T_{\rm D}$. The star takes its energy from Kelvin-Helmholtz (KH) contraction, loosing entropy ($dL_r/dM_r = -Tds/dt > 0$) and increasing T_c. As T_c increases, the opacity in the cen-
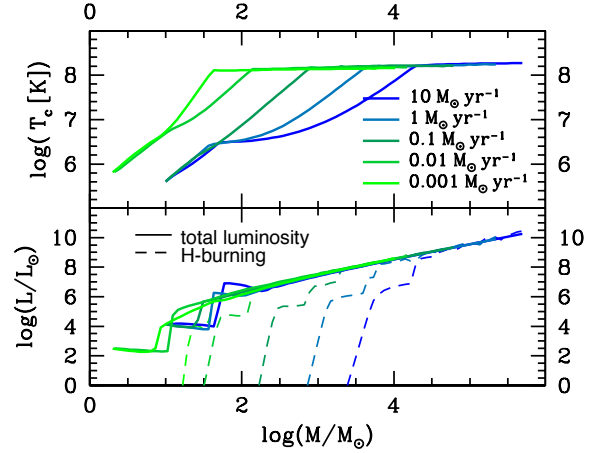

Figure 3. Evolution of the central temperature (upper panel) and of the luminosity (lower panel) as a function of the stellar mass, for models with the indicated accretion rates. On the lower panel, the solid lines indicate the total luminosity, and the dashed lines the contribution from H-burning only.

tre becomes low enough for a radiative core to form and grow in mass. The growth of the radiative core follows the isotherms, which reflects the fact that the transition from convection to radiation is an effect of the temperature increase, through the opacity. Only for $\dot{M} = 10$ M$_\odot$ yr^{-1}, intermediate convective zones survive in between the radiative regions. Since these zones correspond to the Lagrangian layers of the initial seed, we expect their properties to reflect the choice of the initial structure. The reduction of opacity in the central regions produces an increase in the internal luminosity in radiative regions ($dL_r/dM_r > 0$). The entropy produced in these regions is absorbed by the cold external convective layers with high opacity ($dL_r/dM_r < 0$). As the internal temperature increases, the boundary between these two regions moves outwards in mass. When this 'luminosity wave' (Larson 1972; Hosokawa et al. 2010) reaches the stellar surface, the radius increases abruptly, by more than one order of magnitude for $\dot{M} \geq 1$ M$_\odot$ yr^{-1}, by a factor of a few for $\dot{M} \leq 0.01$ M$_\odot$ yr^{-1}. Fig. 4 shows the evolution of the luminosity wave for the model at 0.1 M$_\odot$ yr^{-1}.

In the while, $T_c > T_{\rm D} \simeq 1 - 2 \times 10^6$ K (Fig. 3, upper panel; see also the isotherm of 10^6 K on Fig. 2), and deuterium starts burning: in the radiative core for $\dot{M} \leq 0.1$ M$_\odot$ yr^{-1}, in the central convective zones for $\dot{M} \geq 1$ M$_\odot$ yr^{-1} (Fig. 2). Once deuterium is exhausted in the centre, the D-burning region moves outwards in mass (shell D-burning), following the isotherms (Fig. 2). The convective core that formed in the high-$\dot{M}$ models survives the D exhaustion, but remains confined in the same Lagrangian layers that correspond to the initial seed, and thus contracts with it. Notice that neither this convective zone nor the plateau in central temperature visible on Fig. 3 (at 30M$_\odot < M < 100$M$_\odot$) are due to D-burning, as one could naively believe. Test computations without deuterium confirmed that this features appear in any case. Actually, our computations show that D-burning has no significant impact on the stellar structure of the models described here.

After the luminosity wave has reached the surface, all the layers of the star loose entropy ($dL_r/dM_r = -Tds/dt > 0$).
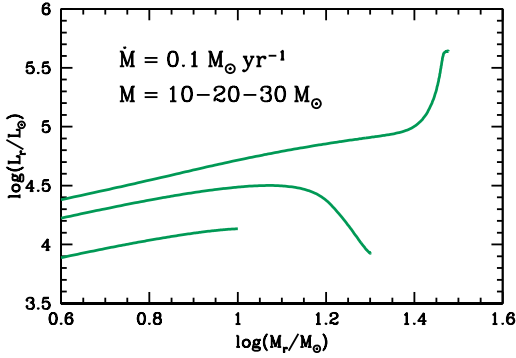
Figure 4. Luminosity wave at 0.1 $M_\odot$ yr^{-1}. The three curves show the internal luminosity profiles at $M = 10$, 20 and 30 $M_\odot$. The first profile corresponds to the fully convective initial model. At the second one, the radiative core has grown to 80% of the total stellar mass, but the stellar radius is still decreasing ($R = 118\,R_\odot$). In the last profile, the luminosity wave has reached the surface, $dL_r/dM_r > 0$ everywhere, and the radius has increased to 821 $R_\odot$.

For low enough accretion rates ($\dot{M} \sim 0.001\,M_\odot$ yr^{-1}), the stellar radius decreases as a consequence, despite the new mass which is continuously accreted, and the star can contract towards the ZAMS. For high $\dot{M}$ however, the entropy losses are not efficient enough to make the stellar radius to decrease. Despite the contraction of all the layers, the new material that lands on the stellar surface makes the stellar radius to increase monotonically for the rest of the evolution.

In order to illustrate the origins of this difference between the low- and high-$\dot{M}$ regime, we plot on Fig. 5 the timescales for accretion and KH contraction. The KH time gives the timescale for thermal adjustment in the stellar interior, and indicates the time it takes for the star to contract towards the ZAMS if accretion stops. We use $t_{KH} = GM^2/RL$ for $M = 500\,M_\odot$, with R and L from the ZAMS of Schaerer (2002). The accretion time is simply $M/\dot{M}$ for the same value of the mass, and gives the timescale of the evolution in the accretion phase. The timescales balance changes according to the accretion rate. For $\dot{M} = 0.001\,M_\odot$ yr^{-1}, the KH time is shorter by one order of magnitude than the accretion time, while for $\dot{M} \geq 0.1\,M_\odot$ yr^{-1} it is longer by one order of magnitude or more (three orders of magnitude for 10 $M_\odot$ yr^{-1}). For the intermediate case $\dot{M} = 0.01\,M_\odot$ yr^{-1}, both timescales are similar. As a consequence, in the low-$\dot{M}$ regime, the star has the time to contract towards the ZAMS before its mass increases significantly, while in the high-$\dot{M}$ regime the mass increases too fast, and the stellar radius grows.

After this point, the behaviour of the various models remains qualitatively different depending on the regime, low- or high-$\dot{M}$. In the low-$\dot{M}$ regime, the internal structure is qualitatively similar to that of stars at present days (see e.g. Haemmerlé et al. 2016). However, due to the lower opacity, the star remains more compact and convective zones are thiner. As a consequence, shell D-burning occurs in the radiative core instead of the convective envelope. In the model at 0.001 $M_\odot$ yr^{-1}, the swelling leads to a maximum radius of 32 $R_\odot$ (instead of 48.6 $R_\odot$ in the present-day case, see model CV2 in Haemmerlé et al. 2016). Then, at $M = 8.5\,M_\odot$, the star becomes fully radiative and contracts. The central temperature increases (Fig. 3, upper panel), triggering
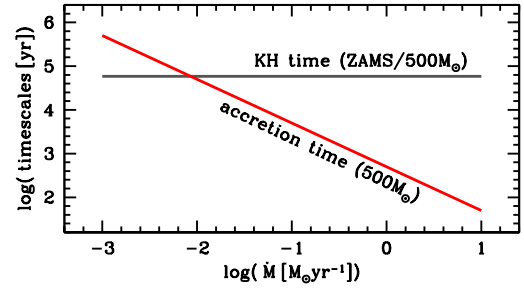

Figure 5. Timescales balance: comparison between the timescales for accretion and KH contraction at $M = 500\,M_\odot$. The KH time is computed using the ZAMS radius and luminosity (Schaerer 2002).

the 3α-reaction. The energy produced by the 3α-reaction remains negligible. The total luminosity is dominated by the gravitational contribution at this stage (KH contraction, $dL_r/dM_r \simeq -T ds/dt$). However, the reaction produces enough ^{12}C in the centre in order to trigger the CNO cycle, which becomes the dominant energy source for the rest of the evolution (Fig. 3, lower panel). As a consequence, a convective core forms at $M = 40\,M_\odot$ and grows in mass (Fig. 2, lower panel), while the central temperature is locked at $T_c = 1.26 \times 10^8$ K due to the thermostatic effect of H-burning (Fig. 3, upper panel). The radius reaches a minimum of 3.3 $R_\odot$ at $M = 50\,M_\odot$, and then grows continuously until the end of the computation, according to the homologous relation $T_c \propto M/R$ and the fact that $T_c \simeq$ cst. At $M = 11\,650\,M_\odot$, numerical convergence becomes too difficult and we stop the computations, while H-burning is still proceeding.

In the high-$\dot{M}$ regime, the structure evolves in a qualitatively different way. Due to the fast mass load at the surface, the radius can not contract and the star remains large. This leads to low temperatures in the outer regions, which keep thus a high opacity and stay convective. Below this convective envelope, intermediate convective zones appear. A high accretion rate favours the formation and the development of these convective regions, because of the timescales balance: the higher the rate, the shorter the time for the star to radiate the entropy contained in the deepest regions before reaching a given mass. For $\dot{M} = 10\,M_\odot$ yr^{-1}, in addition to the convective core described above, an intermediate convective region forms in the Lagrangian layers that were accreted during the swelling (see the iso-mass of 100 $M_\odot$ on the upper panel of Fig. 2). This convective zone results from the accretion of entropy when the luminosity wave crosses the surface. When the peak of the wave approaches the surface ($dL_r/dM_r = -T ds/dt < 0$), the surface entropy increases suddenly. Through the assumption of cold disc accretion, the specific entropy s_{ac} of the material that is accreted increases then. After the passage of the peak, the surface can radiate its entropy efficiently ($dL_r/dM_r = -T ds/dt > 0$), and s_{ac} decreases suddenly. For the layers that are accreted at this stage, the decrease in the accreted entropy results in a negative entropy gradient ($ds/dM_r < 0$), which drives convection. Then, entropy is redistributed on a thermal timescale in the interior, but this mechanism remains inefficient at high $\dot{M}$ because of the timescales balance between the KH and accretion times. This is why this intermediate convective

zone appears only in the model at $\dot{M} > 1$ $M_\odot$ yr^{-1}. Despite the growth of the stellar radius, each Lagrangian layer contracts at this stage. As a consequence, the central temperature increases until H-burning starts (Fig. 3). The physics of H-burning is the same as in the low-$\dot{M}$ regime: the 3α-reaction is triggered first, and produces the ^{12}C that allows the CNO-cycle to operate as the dominant energy source for the rest of the evolution (Fig. 3, lower panel). A convective core forms (Fig. 2), and the central temperature is locked at $T_c \simeq 1.25 - 2 \times 10^8$ K by the thermostatic effect of H-burning (Fig. 3, upper panel). Notice that the higher the accretion rate, the higher the mass at which H-burning starts. This is due to the timescale balance: the higher the rate, the shorter is the accretion time compared to the KH time and thus the higher the mass accreted during the KH contraction towards the ZAMS. Once the convective core has formed, the evolution proceeds in a regular way. The stellar structure is made of three zones: the convective core, that grows in mass and radius along the isotherms ($T \simeq 10^8$ K), the convective envelope, that covers less than 10% of the stellar mass (less than 2% during most of the evolution), and an intermediate radiative region in between. While H burns in the convective core, D burns in a thin shell of the intermediate radiative zone, following the isotherms $T \simeq T_D$. As the stellar mass grows by accretion, the stellar radius continues to increase monotonically. Notice that in the mass-range $200 M_\odot < M < 5 \times 10^4 M_\odot$ the mass-radius relation follows the power-law $R \propto M^{1/2}$ of Hosokawa et al. (2012) (Fig. 6). This relation comes from the facts that the luminosity is close to the Eddington luminosity $L_{Edd} \propto M$ (Fig. 3 and 7), and that the effective temperature is nearly constant along the Hayashi line, so that $L \propto R^2 T_{eff}^4$ gives $R \propto M^{1/2}$.

During this phase, the luminosity is so high that the KH time becomes shorter than the accretion time, despite the growth of the KH time with mass ($t_{KH} = GM^2/RL \propto M^{1/2}$, for $R \propto M^{1/2}$ and $L \propto M$, see Schleicher et al. 2013). However, the structure of massive fast accreting stars is highly non-homologous, so that the argument of the timescales, computed from global quantities with the assumption of homology, is not relevant in this mass range. While most of the layers contract efficiently, a thin surface layer absorbs the entropy radiated by the deep regions and thus cannot contract, despite the short global KH timescale.

Our models run until they reach different final masses, for reasons that are discussed below (Sect. 4.2). However, we notice that none of our models in the high-$\dot{M}$ regime shows a decrease of the stellar radius when the stellar mass exceeds 10^4 $M_\odot$. For $\dot{M} \geq 1$ $M_\odot$ yr^{-1}, our models reach final masses of several 10^5 $M_\odot$, with a radius that is still growing. As a consequence, the effective temperature remains lower than 10^4 K until the stellar mass exceeds 3.5×10^5 $M_\odot$. This is in contrast with the results of previous studies, as discussed below (Sect. 4.3).

In the intermediate case 0.01 $M_\odot$ yr^{-1}, after the swelling, the radiative star starts to contract towards the ZAMS as in the low-$\dot{M}$ regime. But before it contracts significantly, in contrast to the 0.001 $M_\odot$ yr^{-1} case, the Eddington factor exceeds 50% at the surface (Fig. 7). As a consequence, a second swelling occurs. After several oscillations, at a mass of 600 $M_\odot$, Γ_{Edd} exceeds 90%, the radius expands to $\simeq 5000$ $R_\odot$ and the model converges towards the high-$\dot{M}$ regime. Notice that in contrast to the models with
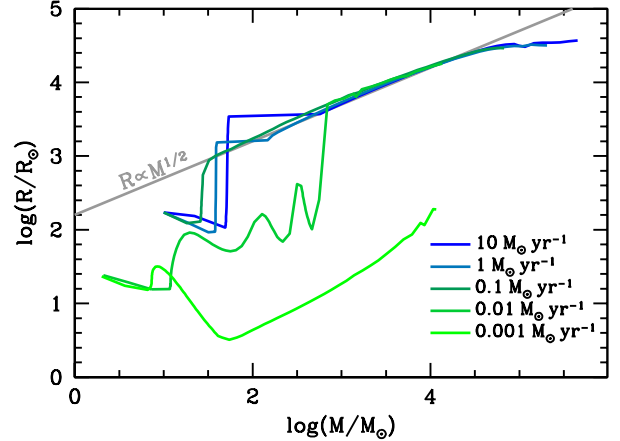

Figure 6. Comparison of the mass-radius relation between our models at indicated accretion rates and the analytic fit $R \propto M^{1/2}$ (Hosokawa et al. 2012).
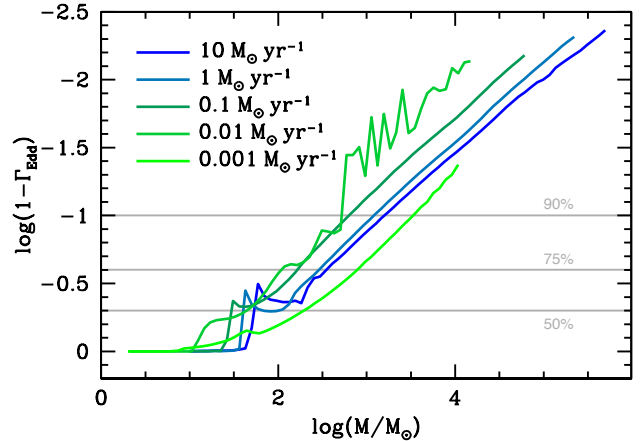

Figure 7. Evolution of the Eddington factor $\Gamma_{Edd} = \nabla P_{rad}/\nabla P$ at the surface for the models with indicated accretion rates. The values $\Gamma_{Edd} = 50$, 75 and 90% are indicated by horizontal grey lines.

$\dot{M} \geq 0.1$ $M_\odot$ yr^{-1}, the model at 0.01 $M_\odot$ yr^{-1} evolves to the red because of the high radiation pressure ($\Gamma_{Edd} > 90\%$), and not because of the high gas pressure related to the high entropy content which cannot be radiated away. In this intermediate case, oscillating between the two regimes, the contribution from radiation pressure is critical in determining the asymptotic behaviour. Notice also that several intermediate convective zones survive between the convective core and the convective envelope in the model at 0.01 $M_\odot$ yr^{-1}. They reflect the accretion history of entropy, in a similar way as the intermediate convective zone of the model at $\dot{M} = 10$ $M_\odot$ yr^{-1}. However, at such low rate, thermal adjustment is efficient enough to redistribute the entropy before these zones join the convective core.

3.3 Ionising feedback and Lyman-Werner flux

Our models show that the effective temperature of a star accreting at $0.001 - 0.1$ $M_\odot$ yr^{-1} depends sensitively on the
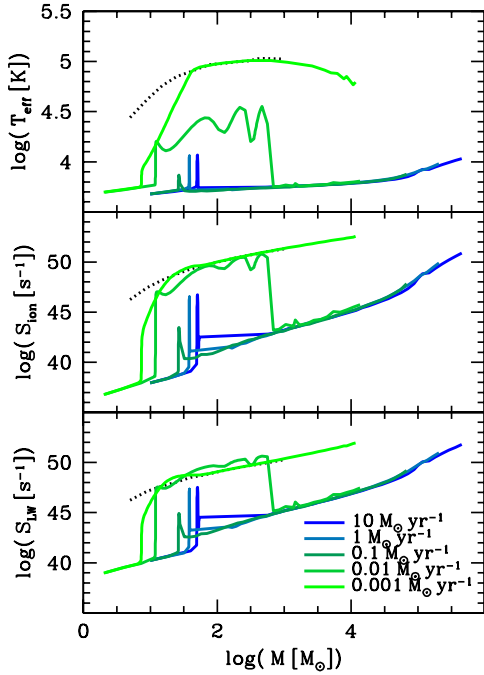
Figure 8. Evolution of the effective temperature (upper panel), ionising photon rate (middle panel) and Lyman-Werner photon rate (bottom panel) as a function of the stellar mass for the models with indicated accretion rates. The black dotted lines correspond to the ZAMS of Schaerer 2002.

rate. To determine if the star can regulate accretion onto itself by radiative feedback, we compute the number of ionising photons per second by integrating the black-body spectrum above the ionising energy:

$$
\begin{aligned}
S_{\mathrm{ion}} &= 4\pi R^2 \int\limits_{h\nu>13.6\,\mathrm{eV}} \frac{F_\nu}{h\nu}\, d\nu \\
&= \frac{8\pi^2 R^2}{c^2 h^2} \int\limits_{h\nu>13.6\,\mathrm{eV}} \frac{(h\nu)^2}{e^{h\nu/kT_{\mathrm{eff}}}-1}\, d\nu
\end{aligned}
\tag{3}
$$

We compute also the Lyman-Werner (LW) flux (11.18 - 13.6 eV):

$$
S_{\mathrm{LW}} = \frac{8\pi^2 R^2}{c^2 h^2} \int\limits_{h\nu=11.18\,\mathrm{eV}}^{13.6\,\mathrm{eV}} \frac{(h\nu)^2}{e^{h\nu/kT_{\mathrm{eff}}}-1}\, d\nu
\tag{4}
$$

The evolution of S_{ion} and S_{LW} as a function of the stellar mass is shown on Fig. 8 for the five accretion rates. The two asymptotic limits in the evolutionary tracks reflect in two asymptotic limits in the ionising and LW fluxes. In the low-$\dot{M}$ case, the ionising photon rate exceeds $10^{45}\,\mathrm{s}^{-1}$ before the stellar mass reaches 20 $\mathrm{M}_\odot$. This increase slows down only when T_{eff} reaches the ZAMS limit. Then S_{ion} grows slower, exceeding $10^{50}\,\mathrm{s}^{-1}$ when the mass is $M > 100$ $\mathrm{M}_\odot$. In the high-$\dot{M}$ regime in contrast, after a short jump corresponding to the adjustment phase to the asymptotic behaviour, the ionising photon rate remains lower than $10^{45}\,\mathrm{s}^{-1}$ until $M = 10^4$ $\mathrm{M}_\odot$, and lower than $10^{50}\,\mathrm{s}^{-1}$ until $M \simeq 3 \times 10^5$ $\mathrm{M}_\odot$. The fluxes grow slowly as the mass increases, following the Hayashi limit. For the intermediate rate 0.01 $\mathrm{M}_\odot\,\mathrm{yr}^{-1}$, the ionising and LW photon rates follow first the ZAMS limit. The oscillations in effective temperature hardly impact the
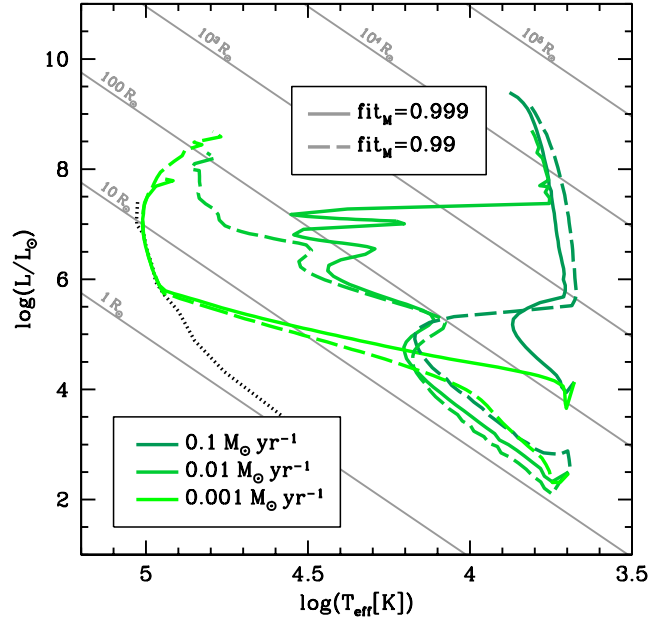
Figure 9. Evolutionary tracks of the models for the indicated accretion rates, for $\mathrm{fit}_M = 0.999$ (solid lines) and 0.99 (dashed lines). The grey straight lines indicate the stellar radius, and the black dotted curve is the ZAMS of Schaerer 2002.

fluxes, because T_{eff} remains in the range $10\,000 - 30\,000$ K. But when the model converges to the Hayashi limit, at $M = 600$ $\mathrm{M}_\odot$, the fluxes switch to the high-$\dot{M}$ regime for the rest of the evolution.

4 DISCUSSION

4.1 Effect of changing the value of fit_M

As mentioned in Sect. 2, the GENEVA code assumes that the energy generation rate is zero and the luminosity profile is flat in the external layers of the star, those above a given value of $\mathrm{fit}_M = M_r/M$. In our models above, we used $\mathrm{fit}_M = 0.999$, except for the case $\dot{M} = 0.001$ $\mathrm{M}_\odot\,\mathrm{yr}^{-1}$ where we used $\mathrm{fit}_M = 0.99$. Here we study the effect of changing the value of fit_M. To that aim, we present models at $\dot{M} > 0.001$ $\mathrm{M}_\odot\,\mathrm{yr}^{-1}$ with $\mathrm{fit}_M = 0.99$, and a model at 0.001 $\mathrm{M}_\odot\,\mathrm{yr}^{-1}$ with $\mathrm{fit}_M = 0.999$. Decreasing fit_M reduces physical consistency, but makes numerical convergence easier. For $\dot{M} < 1$ $\mathrm{M}_\odot\,\mathrm{yr}^{-1}$, models with $\mathrm{fit}_M = 0.99$ are started from the 2 $\mathrm{M}_\odot$ initial protostellar seed, instead of the 10 $\mathrm{M}_\odot$ one (Sect. 3.1). For $\dot{M} = 0.001$ $\mathrm{M}_\odot\,\mathrm{yr}^{-1}$, the model with $\mathrm{fit}_M = 0.999$ is started from the 10 $\mathrm{M}_\odot$ seed.

The evolutionary tracks are shown on Fig. 9 for accretion rates of 0.1, 0.01 and 0.001 $\mathrm{M}_\odot\,\mathrm{yr}^{-1}$. Due to the use of various initial models, the early evolution differs between the $\mathrm{fit}_M = 0.999$ and 0.99 cases. But at the stage where the models at 0.001 and 0.1 $\mathrm{M}_\odot\,\mathrm{yr}^{-1}$ converge to their respective asymptotic behaviours, their evolutionary tracks become nearly independent of fit_M. The slight shift in the tracks at 0.1 $\mathrm{M}_\odot\,\mathrm{yr}^{-1}$ reflects simply the dependence of the exact location of the Hayashi limit on the treatment of the external layers of the star, since this limit results from the opacity in the external layers. The same is true for the
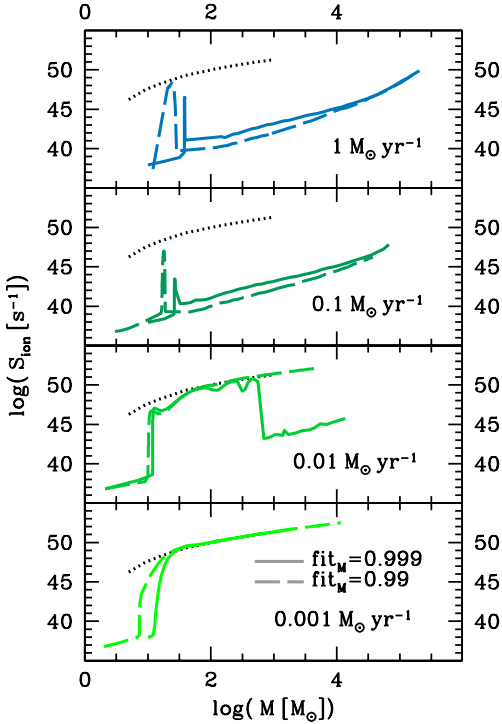
Figure 10. Ionising flux as a function of the stellar mass for the models with indicated accretion rates. On each panel, the solid line corresponds to the model with $\mathrm{fit}_M = 0.999$, and the dashed line to the one with $\mathrm{fit}_M = 0.99$. The black dotted line corresponds to the ZAMS of Schaerer 2002.

1 $M_\odot$ yr^{-1} case, not shown here. In contrast, the asymptotic track in the low-$\dot{M}$ regime (model at 0.001 $M_\odot$ yr^{-1}) is not affected by a change in fit_M, because the location of the ZAMS is fixed by the physics in the centre of the star, and a change in the treatment of the outer layers has no impact. This justifies our choice of $\mathrm{fit}_M = 0.99$ for the model at 0.001 $M_\odot$ yr^{-1} described in Sect. 3.2.

Only for the intermediate case at 0.01 $M_\odot$ yr^{-1}, the asymptotic behaviour differs significantly between $\mathrm{fit}_M = 0.999$ and 0.99. After several oscillations in T_{eff}, when the model at $\mathrm{fit}_M = 0.999$ converges to the Hayashi limit in the red, with $T_{\mathrm{eff}} < 10^4$ K, the model at $\mathrm{fit}_M = 0.99$ remains in the blue, close to the low-$\dot{M}$ tracks, with $T_{\mathrm{eff}} \simeq 70000$ K. Thus at this intermediate rate, the asymptotic behaviour is switched from one limit to the other by a change in fit_M. We notice also that before the convergence to the asymptotic track, the amplitude of the oscillations in T_{eff} is reduced by the decrease in fit_M.

In order to study how this effect impacts the ionising flux, we compute S_{ion} according to Eq. (3) for the same models. The result is shown on Fig. 10. As expected from the evolutionary tracks, for $\dot{M} \geq 0.1$ $M_\odot$ yr^{-1} and $\dot{M} = 0.001$ $M_\odot$ yr^{-1}, S_{ion} is nearly unaffected by a change in fit_M. Only in the intermediate case 0.01 $M_\odot$ yr^{-1}, S_{ion} differs between models at $\mathrm{fit}_M = 0.999$ and 0.99. The reduction of the amplitude of the T_{eff}-oscillations in the model at $\mathrm{fit}_M = 0.99$ makes S_{ion} to follow the ZAMS limit closer. But more importantly, as the model with $\mathrm{fit}_M = 0.999$ converges to the high-$\dot{M}$ regime, the corresponding value of S_{ion} decreases suddenly by 8 orders of magnitude, from 10^{51} to

10^{43} s^{-1}. At the same stage, the model with $\mathrm{fit}_M = 0.99$ remains in the blue, with S_{ion} growing slowly ($S_{\mathrm{ion}} > 10^{50}$ s^{-1}). The 8 orders of magnitude difference is maintained as the stellar mass approaches 10^4 $M_\odot$.

This example shows that the choice of fit_M is critical in order to determine properly the ionising properties of stars accreting at a rate between 0.001 and 0.1 $M_\odot$ yr^{-1}. Difficulties in numerical convergence make it impossible to use $\mathrm{fit}_M > 0.999$. However, the models described above show that an increase in fit_M leads to larger radii and lower effective temperatures. But the Hayashi limit prevents T_{eff} to decrease under 5000 – 6000 K. Since our model at $\dot{M} = 0.01$ $M_\odot$ yr^{-1} and $\mathrm{fit}_M = 0.999$ reaches the Hayashi limit at 600 $M_\odot$, we do not expect a further increase in fit_M to modify the track in the supermassive range. Actually, regarding the above examples, one can expect convergence to the high-$\dot{M}$ asymptotic track to occur earlier at higher fit_M. Thus a further increase in fit_M could potentially reduce the value of $\dot{M}_{\mathrm{crit}}$ closer to 0.001 $M_\odot$ yr^{-1}, and bring definitely the intermediate 0.01 $M_\odot$ yr^{-1} rate to the high-$\dot{M}$ range. An accurate treatment of the external layers of the accreting star is thus required in order to determine the exact value of $\dot{M}_{\mathrm{crit}}$, but our models suggest a value closer to 0.005 $M_\odot$ yr^{-1} than to 0.05 $M_\odot$ yr^{-1}.

4.2 Final mass at the onset of the collapse

Despite the absence of hydrodynamics in our models, one can estimate the stage at which the GR instability triggers the collapse using the polytropic criterion of Chandrasekhar (1964) (though see Woods et al. 2017). According to this criterion, the star becomes unstable when the adiabatic index Γ is reduced under a critical value Γ_{crit}. For a classical star ($GM_r/rc^2 = 0$), this critical value is simply 4/3. The first order relativistic development ($GM_r/rc^2 << 1$) in the polytropic case gives

$$\Gamma_{\mathrm{crit}} = \frac{4}{3} + K \frac{2GM_r}{rc^2} \ , \tag{5}$$

where K is a constant that depends on the polytropic index ($K \simeq 1.12$ for $n = 3$). For a purely radiation-supported star ($P = P_{\mathrm{rad}}$, $P_{\mathrm{gas}} = 0$), the adiabatic index is exactly 4/3, and the star is unstable. The first order development in terms of $\beta = P_{\mathrm{gas}}/P$, the ratio of gas pressure to total pressure, is

$$\Gamma = \frac{4}{3} + \frac{\beta}{6} \ . \tag{6}$$

Thus for stars that are dominated by radiation ($\beta << 1$), the stability criterion $\Gamma > \Gamma_{\mathrm{crit}}$ can be expressed as

$$\frac{\beta}{6} > K \frac{2GM_r}{rc^2} \ . \tag{7}$$

The two members of Eq. (7) are compared in Fig. 11 for our models with $\dot{M} = 10$, 1 and 0.1 $M_\odot$ yr^{-1} at various stellar masses, using $K = 1.12$. The right column shows the internal profiles of these quantities at the end of the computations, while the left one shows it at an earlier stage. The regions that are unstable according to the polytropic criterion are also shown as red areas on Fig. 2. In all the cases, the stellar structure consist in a convective core (coloured regions at the left-hand sides of each plot), an intermediate radiative zone (grey regions) and a convective envelope
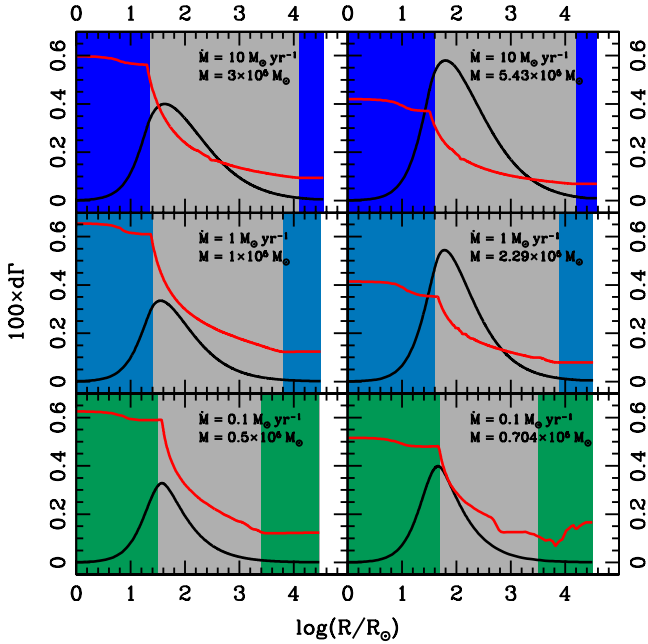
Figure 11. Polytropic criterion of GR stability for $\dot{M} =$ 10 $M_\odot$ yr^{-1} (upper row), 1 $M_\odot$ yr^{-1} (middle row) and 0.1 $M_\odot$ yr^{-1} (bottom row). On each plot, the black curves are the internal profiles of the first order GR correction to $\Gamma_{\rm crit}$ (Eq. 5) for $K = 1.12$ ($n = 3$). The red curves correspond to the internal profiles of the first order correction to Γ in terms of β (Eq. 6). The coloured and grey areas are respectively convective and radiative zones. The right column shows the profiles at the end of the computation, while the left one shows it a an earlier stage, corresponding to the indicated masses.

(coloured region at the right-hand sides). Since the stability criterion of Eq. (7) is based on polytropic structures, the changes in the polytropic indices between the various regions of the star complicates the analysis. In each case, most of the mass of the star is contained in the radiative region, so that one could naively expect the $n = 3$ criterion to be relevant. However, the high-entropy accreted envelope is not approximated by an $n = 3$ polytrope in the present case. Moreover, we notice that the regions that are unstable according to the criterion are located deep in the radiative zone, close to the edge of the convective core, where the first order relativistic correction to $\Gamma_{\rm crit}$ has its maximum. In the model at 10 $M_\odot$ yr^{-1}, the criterion indicates instability in the radiative zone at $M = 261\,000\,M_\odot$. As evolution proceeds, the 'unstable' zones grow, joining eventually the convective core. In the model at 1 $M_\odot$ yr^{-1}, the criterion indicates instability at $M = 116\,000\,M_\odot$. The 0.1 $M_\odot$ yr^{-1} model was stopped at $M = 0.7 \times 10^5\,M_\odot$ for numerical reasons, when $\beta/6$ was approaching $1.12 \times 2GM_r/rc^2$ close to the convective core. We summarise these results in Table 1. The final masses are compared on Fig. 13 with those of Woods et al. (2017) and Umeda et al. (2016), as discussed below (Sect. 4.3).

4.3 Comparison with previous studies

The evolution of Pop III stars under high accretion rates has been computed by several authors under various physical conditions. Omukai & Palla (2001, 2003) and Hosokawa

Table 1. Final masses of the models of indicated accretion rates. The first line is the accretion rate ($\dot{M}$), the second one ($M_{\rm crit}$) contains the mass at which instability appears according to the polytropic criterion with index $n = 3$, and the third one ($M_{\rm fin}$) shows the final mass of our runs.

$\dot{M} =$	0.1	1	10	$M_\odot$ yr^{-1}
$M_{\rm crit} =$		1.16	2.61	$\times 10^5\,M_\odot$
$M_{\rm fin} =$	0.70	2.29	5.43	$\times 10^5\,M_\odot$

et al. (2012) used rates in the range 0.001 - 1 $M_\odot$ yr^{-1} to produce models towards 1000 $M_\odot$ with the assumption of spherical accretion, in which all the entropy of the accretion shock is advected in the stellar interior. This assumption is expected to produce stars that are more bloated than in the disc case, due to their high amount of internal entropy. In these models, stars evolve as red supergiant protostars along the Hayashi line if $\dot{M} > \dot{M}_{\rm crit}$, contract to the ZAMS if $\dot{M} < \dot{M}_{\rm crit}$, and oscillate in $T_{\rm eff}$ between these two limits if $\dot{M} \simeq \dot{M}_{\rm crit}$. Omukai & Palla (2001, 2003) obtained a critical value of $\dot{M}_{\rm crit} = 0.004\,M_\odot$ yr^{-1}. In Hosokawa et al. (2012), a model at $\dot{M} = 0.006\,M_\odot$ yr^{-1} oscillates in $T_{\rm eff}$ without converging to the Hayashi limit before the end of their computation, at $M = 600 - 700\,M_\odot$. Omukai & Palla (2003) concluded that this expansion indicates the end of the accretion phase, since radiation pressure close to the Eddington limit is expected to reverse an accretion flow having a spherical symmetry. In contrast, at lower rates, the star contracts towards the ZAMS despite accretion. But at the high effective temperatures of the ZAMS, the ionising effect of the radiation field becomes significant, and a large H II region, with high pressure, is expected to form around the star, preventing accretion above $\sim 50\,M_\odot$ (Hosokawa et al. 2011).

All these computations were stopped at 1000 $M_\odot$ due to convergence difficulties in the code used, that solves the structure equations with a shooting method. Hosokawa et al. (2013) used instead the numerical code STELLAR (Yorke & Bodenheimer 2008), based on the Henyey method, like the GENEVA code, to push the computations towards higher masses. In contrast to the previous studies, entropy is accreted according to cold disc accretion, like in our models. They confirmed that at rates above $\dot{M}_{\rm crit}$ the star evolves as a red supergiant protostar, with $T_{\rm eff} < 10^4$ K. But the value they obtain for $\dot{M}_{\rm crit}$ exceeds 0.01 $M_\odot$ yr^{-1}, in contrast to Omukai & Palla (2001, 2003). Indeed, after several oscillations in $T_{\rm eff}$, their model at 0.01 $M_\odot$ yr^{-1} remains in the blue until the end of their computation, at $M \simeq 2000\,M_\odot$ and $L \simeq 10^8\,L_\odot$. Only at 0.1 $M_\odot$ yr^{-1} the star converges to the Hayashi limit, already at $M \simeq 30\,M_\odot$, and evolves then as a red supergiant protostar. Exploring the supermassive range, the supergiant models of Hosokawa et al. (2013) start to decrease in radius at $M \simeq 3 \times 10^4\,M_\odot$. At this point, the effective temperature grows, which could potentially lead to the formation of an H II region during further evolution, not followed in their models. Their computation stops at $10^5\,M_\odot$. Although their code does not include the GR correction in general, they computed a few test-models with it, and found the correction to be negligible below $10^5\,M_\odot$, when they stopped their computations. The difference in the exact value of $\dot{M}_{\rm crit}$ between Omukai & Palla (2001, 2003) and

Hosokawa et al. (2013) is expected to come from the change in the accretion of entropy, between hot spherical and cold disc accretion. Indeed, the reduction of the entropy accreted in the disc case compared to the spherical case makes accreting stars more compact, so that a higher rate is needed in order to produce red supergiant protostars. Thus the results of Omukai & Palla (2001, 2003) and Hosokawa et al. (2013) indicate $\dot{M}_{crit} \simeq 0.004\ M_\odot\ yr^{-1}$ for spherical accretion and $\dot{M}_{crit} > 0.01\ M_\odot\ yr^{-1}$ for disc accretion.

Notice that Schleicher et al. (2013), using analytical considerations based on timescales comparisons, obtained that stars accreting at a rate above $0.14\ M_\odot\ yr^{-1}$ continue to expand in radius until the mass reaches $10^6\ M_\odot$, in contrast with the results of Hosokawa et al. (2013).

Our models, based on cold disc accretion, explore the highest mass-range, above $10^5\ M_\odot$, until the star collapses into a black hole. We confirm the main features obtained in the studies mentioned above: stars accreting above a critical rate $\dot{M}_{crit}$ evolve as red supergiants along the Hayashi limit, while under $\dot{M}_{crit}$ they contract towards the ZAMS. However, two differences appear between our models and those of Hosokawa et al. (2013). First, our results indicate $\dot{M}_{crit} < 0.01\ M_\odot\ yr^{-1}$, since after several oscillations in effective temperature our model at $0.01\ M_\odot\ yr^{-1}$ converges to the Hayashi limit and evolve as a red supergiant protostar when its mass exceeds $600\ M_\odot$. This fact suggests that $\dot{M}_{crit}$ is closer to the value obtained by Omukai & Palla (2001, 2003) for spherical accretion than to the one obtained by Hosokawa et al. (2013) in the disc case. Our numerical experiment described in Sect. 4.1 suggests that this discrepancy is related to the treatment of the energy equation in the external layers of the star. Indeed, neglecting the production of energy on the external 1% of the stellar mass gives an evolutionary track at $0.01\ M_\odot\ yr^{-1}$ which is similar as that of Hosokawa et al. (2013). In other words, our models show that an accurate treatment of the energy equation in the external layers can reduce the value of $\dot{M}_{crit}$ by nearly one order of magnitude, from ~ 0.05 to $\sim 0.005\ M_\odot\ yr^{-1}$. Of course, this conclusion concerns the mass range $M \gtrsim 600\ M_\odot$. A star that would effectively accrete at $0.01\ M_\odot\ yr^{-1}$ during its whole accretion phase would produce a strong UV feedback during the early phase ($M < 600\ M_\odot$), that might disrupt the accretion flow. Knowing the detailed impact of such a UV feedback on the accretion flow during this phase would require a self-consistent treatment of stellar evolution and hydrodynamics of the accretion flow. Such a study has been performed by Hosokawa et al. (2011), who considered a pre-stellar cloud cooled by H_2 molecules, and thus having lower temperature and accretion rate ($\sim 0.001\ M_\odot\ yr^{-1}$). In this study, the accretion process ended after the central star accreted $42\ M_\odot$. Interestingly, the duration of the accretion phase in Hosokawa et al. (2011) (7×10^4 yr, see their Fig.2, panel d) is slightly longer than the duration of the phase with strong UV feedback in our $0.01\ M_\odot\ yr^{-1}$ model (6×10^4 yr). Thus it is not clear if this strong UV feedback would effectively stop the accretion process in such a timescale. Moreover, our results suggest that a star accreting at a rate decreasing with time, with $\dot{M} > 0.01\ M_\odot\ yr^{-1}$ while $M < 600\ M_\odot$, and $\dot{M} = 0.01\ M_\odot\ yr^{-1}$ for $M > 600\ M_\odot$ would keep a negligible UV feedback. This is in contrast to the results of previous studies, and thus our results extend
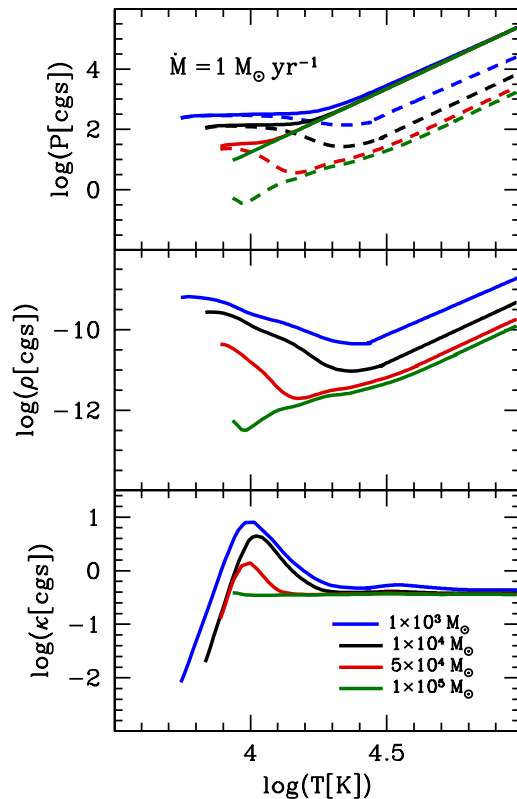

Figure 12. Internal profiles of the pressure (upper panel), the mass density (middle panel) and the opacity (lower panel) at the surface (under the photosphere) of the model with $\dot{M} = 1\ M_\odot\ yr^{-1}$ at the indicated masses. The horizontal coordinate is the temperature, that increases inwards. On the upper panel, the solid lines correspond to the total pressure, while the dashed lines show the gas pressure only.

the range of accretion rates at which the ionising feedback remains negligible.

The second difference between our models and those of Hosokawa et al. (2013) concerns the evolution in the supermassive range. In contrast to the models of Hosokawa et al. (2013), our supergiant models never show a decrease of the stellar radius at $M > 10^4\ M_\odot$. **The radius continues to expand until the highest mass ($\simeq 5 \times 10^5\ M_\odot$ for $\dot{M} = 10\ M_\odot\ yr^{-1}$), in contrast to Hosokawa et al. (2013), who obtained a decrease in the radius for $M \gtrsim 2 \times 10^4\ M_\odot$.** Indeed, the fact that T_{eff} is nearly constant along the Hayashi line comes from the sensitive temperature dependence of opacity from H^- ions. But at $M \gtrsim 10^4\ M_\odot$, the decrease of the mass-density in the outer expanded layers makes the H^- ions to disappear (Fig. 12). For this reason, T_{eff} is not locked anymore and can grow, which makes the mass-radius relation to deviate from $R \propto M^{1/2}$ for $M \gtrsim 10^5\ M_\odot$ (Fig. 6). However, the increase in T_{eff} does not necessarily reflects in a decrease of the radius, since the luminosity continues to grow. The increase in T_{eff} remains much more modest in our models than in those of Hosokawa et al. (2013), and thus it does not result in the decrease of the radius. In Hosokawa et al. (2013), T_{eff} reaches 10^4 K already at $M = 10^5\ M_\odot$, while in our models it occurs only when the star is five times more massive ($M \simeq 5 \times 10^5\ M_\odot$). Thus our mod-
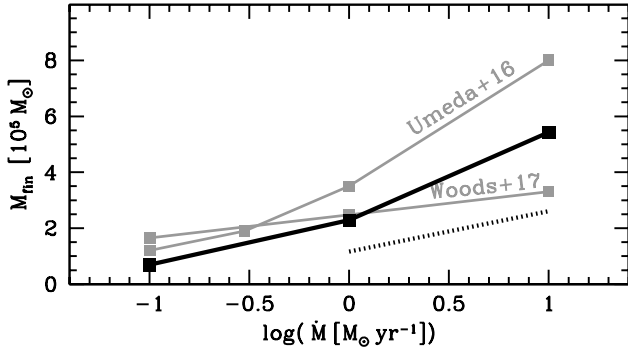
Figure 13. Final masses as a function of the accretion rate. The black curves show the results of the present work: the solid line corresponds the final mass of our runs, and the dotted line to the mass at which the polytropic criterion indicates instability for $n = 3$. The grey curves are the final masses according to previous studies (Woods et al. 2017; Umeda et al. 2016).

els show that we do not expect the ionising flux to grow significantly, even when the stellar mass exceeds $10^5\,\mathrm{M}_\odot$. This result extends the mass-range in which stars accreting at high rate do not significantly ionise their surrounding.

Recently, Umeda et al. (2016) presented models of Pop III stars accreting at rates $0.1 - 0.3 - 1 - 10\,\mathrm{M}_\odot\,\mathrm{yr}^{-1}$, including the post-Newtonian correction. Their model run until final masses of $1.2 - 1.9 - 3.5 - 8.0 \times 10^5\,\mathrm{M}_\odot$, respectively. **At these masses, the star collapses into a black hole through the GR instability.** No evolutionary track of their models are provided, and we do not know if expansion stops in their model when the stellar mass exceeds $10^4\,\mathrm{M}_\odot$.

In a previous paper (Woods et al. 2017), we used the KEPLER code to follow the evolution of Pop III stars accreting at high rates until the final collapse. Since the KEPLER code includes hydrodynamics, the onset of the collapse can be followed self-consistently, without the use of the polytropic criterion **considered in the present work** The collapse is triggered at masses of $1.5 - 3.3 \times 10^5\,\mathrm{M}_\odot$ for $\dot{M} = 0.1 - 10\,\mathrm{M}_\odot\,\mathrm{yr}^{-1}$.

The final masses are shown on Fig. 13 as a function of the accretion rate, for the various studies. Models of Umeda et al. (2016), of Woods et al. (2017) and of the present work all agree with the fact that the mass at collapse remains in the same order of magnitude ($\sim 1 - 8 \times 10^5\,\mathrm{M}_\odot$) over the two orders of magnitude range from 0.1 to $10\,\mathrm{M}_\odot\,\mathrm{yr}^{-1}$ in $\dot{M}$, with a slight increase as a function of $\dot{M}$. However, strong discrepancies appear in the exact values of the mass. Umeda et al. (2016) obtained final masses that are larger to our M_{fin} by a factor 1.5, nearly independently of the accretion rate. Thus, despite the discrepancies in M_{fin}, the dependence of M_{fin} on $\dot{M}$ is similar between Umeda et al. (2016) and us. In Woods et al. (2017), the slope of the curve ($\dot{M}, M_{\mathrm{fin}}$), i.e. the dependence of M_{fin} on $\dot{M}$, is weaker than in the present models and those of Umeda et al. (2016). In particular, for $\dot{M} = 10\,\mathrm{M}_\odot\,\mathrm{yr}^{-1}$, the final mass in Woods et al. (2017) is only 60% of that of the present work.

The validity of the polytropic criterion used in the present work can be questioned, since the stellar structures considered here are not polytropes. Indeed, Woods et al.

(2017) showed that with a self-consistent treatment of hydrodynamics the star remains stable well after the polytropic criterion indicates instability in the convective core. This suggests that the criterion provides only a lower limit for the final mass of SMSs.

Moreover, the final masses of our runs are not necessary the masses at collapse, first because numerical instability could be responsible for the impossibility to make the code to converge at higher masses, second because the GR instability is a pulsational instability (Chandrasekhar 1964). Marginal stability allows hydrostatic equations to be solved during that stage, and a hydrostatic code can evolve through this phase without noticing anything. As a consequence, a fully consistent treatment of hydrodynamics is necessary to capture the GR instability.

A detailed treatment of the accretion of entropy and of convection itself are expected significantly effect the results. Any departure from cold disc accretion could impact the stellar structure, in particular at high rates, for which the accretion history of entropy plays a more important role than internal entropy redistribution in shaping the entropy gradient, as described in Sect. 3.2. Since the entropy gradient determines the presence of convection, a change in the accretion of entropy could impact significantly the mass at which the collapse occurs. More importantly, the treatment of convection, based on the mixing-length theory, appears as critical. In the present work, the triggering of convection is based on the Schwarzschild criterion. The use of the Ledoux criterion, that takes the chemical gradient into account as a stabilizing effect, favours purely radiative transport and reduces convective regions. Moreover, we do not include overshooting in our models. Including overshooting would increase the mass of the convective core, and thus decrease potentially the collapse masses. Actually, a comparison between the models of the present study and those of Woods et al. (2017) shows that for $\dot{M} \geq 1\,\mathrm{M}_\odot\,\mathrm{yr}^{-1}$ the convective core in our models is less extended than in those of Woods et al. (2017), due to the various treatment of convection and of the accretion of entropy. While for $\dot{M} = 0.1\,\mathrm{M}_\odot\,\mathrm{yr}^{-1}$ the mass of the convective core at a given stellar mass is identical between both studies, for $\dot{M} = 1\,\mathrm{M}_\odot\,\mathrm{yr}^{-1}$ it is larger by 25% in Woods et al. (2017) compared to the present study. For $\dot{M} = 10\,\mathrm{M}_\odot\,\mathrm{yr}^{-1}$, the ratio of the masses of convective cores at a given mass is as high as 2. This fact contributes also to explain the discrepancies in the final masses. As a consequence, a precise estimation of the stellar mass at collapse is currently problematic due to the difficulties in modeling self-consistently convection and the accretion of entropy. One can interpret the various curves of Fig. 13 as providing the envelope of the real $\dot{M} - M_{\mathrm{fin}}$ relation.

5   CONCLUSION

In the present work, we described new models of Pop III protostars accreting at high rates ($0.001 - 10\,\mathrm{M}_\odot\,\mathrm{yr}^{-1}$) towards the mass at which the GR instability is expected to trigger the collapse into a black hole. We described the evolutionary tracks and internal structures of these models, and studied the properties of their radiative feedback. We confirm the results of previous studies that stars accreting at a rate above a critical value $\dot{M}_{\mathrm{crit}}$ evolve as red supergiants,

following the Hayashi limit in the red part of the HR diagram with a weak ionising feedback, while for lower rates the star contracts towards the ZAMS in the blue with a strong ionising feedback.

In contrast to previous studies, our models show that Pop III protostars accreting at rates $\gtrsim 0.1$ M$_\odot$ yr^{-1} continue to expand in radius in the highest mass-range ($> 10^5$ M$_\odot$), until it reaches GR instability. Thus no significant increase in the ionising effect of the radiation field are expected in this mass-range as long as rapid accretion proceeds. In addition, compared to previous studies, our models reduce the value of $\dot{M}_{\rm crit}$ **in the later stage** ($M \gtrsim 600$ M$_\odot$) in the case of cold disc accretion, by nearly one order of magnitude, from ~ 0.05 to ~ 0.005 M$_\odot$ yr^{-1}. Thus our results extend the range of masses and accretion rates at which the ionising feedback remains negligible.

Using the polytropic criterion of Chandrasekhar (1964) for GR instability, we estimated the mass at which the protostar collapses into a black hole. We obtained collapse masses that remain in the same order of magnitude (ranging from 0.7 to 5.5×10^5 M$_\odot$) for accretion rates that varies in the two orders of magnitude range $0.1 - 10$ M$_\odot$ yr^{-1}. Inside this interval, the collapse mass increases with $\dot{M}$. Our final masses are in the interval of the various values obtained in previous studies, and the dependence on $\dot{M}$ is qualitatively in agreement with these studies. Discrepancies remain in the exact value of the mass at collapse. We interpret them as the result of the various treatment of entropy accretion and of convection, and in particular the use of the polytropic criterion instead of a fully consistent treatment of the hydrodynamics.

APPENDIX A: TABLES

Tables A to A display the age, mass, radius, luminosity, effective temperature, ionising flux and Lyman-Werner flux. The ionising and LW fluxes are computed from Eq. (3) and (4). The age is counted since $M = 0$, i.e. $t = M/\dot{M}$. The time-steps are computed so that the differences in $\log(L/L_\odot)$ and $\log T_{\rm eff}$ between two consecutive points does not exceed 0.1 and 0.025, respectively.

ACKNOWLEDGEMENTS

REFERENCES

Agarwal B., Khochfar S., Johnson J. L., Neistein E., Dalla Vecchia C., Livio M., 2012, MNRAS, 425, 2854
Agarwal B., Johnson J. L., Zackrisson E., Labbe I., van den Bosch F. C., Natarajan P., Khochfar S., 2016, MNRAS, 460, 4003
Alvarez M. A., Wise J. H., Abel T., 2009, ApJ, 701, L133
Appenzeller I., Fricke K., 1972a, A&A, 18, 10
Appenzeller I., Fricke K., 1972b, A&A, 21, 285
Becerra F., Greif T. H., Springel V., Hernquist L. E., 2015, MNRAS, 446, 2380
Behrend R., Maeder A., 2001, A&A, 373, 190
Bernasconi P. A., Maeder A., 1996, A&A, 307, 829
Chandrasekhar S., 1964, ApJ, 140, 417
Dijkstra M., Ferrara A., Mesinger A., 2014, MNRAS, 442, 2036
Eggenberger P., Meynet G., Maeder A., Hirschi R., Charbonnel C., Talon S., Ekström S., 2008, Ap&SS, 316, 43
Fricke K. J., 1973, ApJ, 183, 941
Fuller G. M., Woosley S. E., Weaver T. A., 1986, ApJ, 307, 675
Haemmerlé L., Eggenberger P., Meynet G., Maeder A., Charbonnel C., 2013, A&A, 557, A112
Haemmerlé L., Eggenberger P., Meynet G., Maeder A., Charbonnel C., 2016, A&A, 585, A65
Hartwig T., et al., 2016, MNRAS, 462, 2184
Hirano S., Hosokawa T., Yoshida N., Umeda H., Omukai K., Chiaki G., Yorke H. W., 2014, ApJ, 781, 60
Hosokawa T., Yorke H. W., Omukai K., 2010, ApJ, 721, 478
Hosokawa T., Omukai K., Yoshida N., Yorke H. W., 2011, Science, 334, 1250
Hosokawa T., Omukai K., Yorke H. W., 2012, ApJ, 756, 93
Hosokawa T., Yorke H. W., Inayoshi K., Omukai K., Yoshida N., 2013, ApJ, 778, 178
Iben Jr. I., 1963, ApJ, 138, 1090
Iglesias C. A., Rogers F. J., 1996, ApJ, 464, 943
Inayoshi K., Haiman Z., 2014, MNRAS, 445, 1549
Inayoshi K., Omukai K., 2012, MNRAS, 422, 2539
Inayoshi K., Visbal E., Kashiyama K., 2015, MNRAS, 453, 1692
Inayoshi K., Haiman Z., Ostriker J. P., 2016, MNRAS, 459, 3738
Johnson J. L., Whalen D. J., Fryer C. L., Li H., 2012, ApJ, 750, 66
Larson R. B., 1972, MNRAS, 157, 121
Latif M. A., Schleicher D. R. G., Schmidt W., Niemeyer J., 2013a, MNRAS, 433, 1607
Latif M. A., Schleicher D. R. G., Schmidt W., Niemeyer J. C., 2013b, MNRAS, 436, 2989
Mortlock D. J., et al., 2011, Nature, 474, 616
Omukai K., Palla F., 2001, ApJ, 561, L55
Omukai K., Palla F., 2003, ApJ, 589, 677
Osaki Y., 1966, PASJ, 18, 384
Palla F., Stahler S. W., 1992, ApJ, 392, 667
Pallottini A., et al., 2015, MNRAS, 453, 2465
Park K., Ricotti M., 2011, ApJ, 739, 2
Pezzulli E., Valiante R., Schneider R., 2016, MNRAS, 458, 3047
Regan J. A., Johansson P. H., Haehnelt M. G., 2014, MNRAS, 439, 1160
Sakurai Y., Hosokawa T., Yoshida N., Yorke H. W., 2015, MNRAS, 452, 755
Sakurai Y., Inayoshi K., Haiman Z., 2016, MNRAS, 461, 4496
Schaerer D., 2002, A&A, 382, 28
Schleicher D. R. G., Palla F., Ferrara A., Galli D., Latif M., 2013, A&A, 558, A59
Shapiro S. L., Teukolsky S. A., 1979, ApJ, 234, L177
Smidt J., Whalen D. J., Johnson J. L., Li H., 2017, arXiv:1703.00449,
Sobral D., Matthee J., Darvish B., Schaerer D., Mobasher B., Röttgering H. J. A., Santos S., Hemmati S., 2015, ApJ, 808, 139
Umeda H., Hosokawa T., Omukai K., Yoshida N., 2016, ApJ, 830, L34
Unno W., 1971, PASJ, 23, 123
Volonteri M., Silk J., Dubus G., 2015, ApJ, 804, 148
Whalen D. J., Fryer C. L., 2012, ApJ, 756, L19
Whalen D., Abel T., Norman M. L., 2004, ApJ, 610, 14
Woods T. E., Heger A., Whalen D. J., Haemmerlé L., Klessen R. S., 2017, ApJ, 842, L6
Wu X.-B., et al., 2015, Nature, 518, 512

Table A1. Model at $\dot{M} = 10$ M$_\odot$ yr^{-1}

age [yr]	log($M/$M$_\odot$)	log($R/$R$_\odot$)	log($L/$L$_\odot$)	log($T_{\rm eff}$[K])	log($S_{\rm ion}$[s^{-1}])	log($S_{\rm LW}$[s^{-1}])
1.000e+00	1.000e+00	2.235e+00	4.133e+00	3.678e+00	3.794e+01	4.022e+01
3.376e+02	1.348e+00	2.187e+00	4.137e+00	3.703e+00	3.857e+01	4.081e+01
3.394e+02	1.602e+00	2.070e+00	4.002e+00	3.728e+00	3.912e+01	4.120e+01
3.403e+02	1.693e+00	2.029e+00	4.023e+00	3.753e+00	3.984e+01	4.175e+01
3.403e+02	1.693e+00	2.035e+00	4.127e+00	3.776e+00	4.048e+01	4.233e+01
3.403e+02	1.694e+00	2.038e+00	4.230e+00	3.800e+00	4.113e+01	4.285e+01
3.403e+02	1.695e+00	2.042e+00	4.330e+00	3.824e+00	4.173e+01	4.336e+01
3.403e+02	1.695e+00	2.046e+00	4.434e+00	3.847e+00	4.227e+01	4.383e+01
3.403e+02	1.696e+00	2.051e+00	4.540e+00	3.872e+00	4.282e+01	4.430e+01
3.403e+02	1.696e+00	2.056e+00	4.641e+00	3.894e+00	4.332e+01	4.469e+01
3.403e+02	1.697e+00	2.062e+00	4.742e+00	3.917e+00	4.383e+01	4.508e+01
3.403e+02	1.697e+00	2.069e+00	4.846e+00	3.939e+00	4.425e+01	4.547e+01
3.403e+02	1.698e+00	2.076e+00	4.953e+00	3.962e+00	4.471e+01	4.582e+01
3.404e+02	1.698e+00	2.085e+00	5.059e+00	3.984e+00	4.510e+01	4.617e+01
3.404e+02	1.699e+00	2.096e+00	5.162e+00	4.005e+00	4.549e+01	4.647e+01
3.404e+02	1.700e+00	2.109e+00	5.267e+00	4.024e+00	4.583e+01	4.677e+01
3.404e+02	1.700e+00	2.126e+00	5.369e+00	4.041e+00	4.614e+01	4.702e+01
3.404e+02	1.701e+00	2.148e+00	5.470e+00	4.056e+00	4.639e+01	4.724e+01
3.404e+02	1.702e+00	2.179e+00	5.573e+00	4.065e+00	4.660e+01	4.742e+01
3.404e+02	1.704e+00	2.228e+00	5.675e+00	4.067e+00	4.672e+01	4.753e+01
3.404e+02	1.706e+00	2.309e+00	5.775e+00	4.051e+00	4.663e+01	4.751e+01
3.405e+02	1.709e+00	2.496e+00	5.875e+00	3.983e+00	4.592e+01	4.697e+01
3.406e+02	1.716e+00	3.005e+00	5.980e+00	3.754e+00	4.180e+01	4.378e+01
3.406e+02	1.717e+00	3.096e+00	6.081e+00	3.734e+00	4.141e+01	4.342e+01
3.406e+02	1.718e+00	3.165e+00	6.184e+00	3.726e+00	4.130e+01	4.339e+01
3.406e+02	1.719e+00	3.218e+00	6.284e+00	3.724e+00	4.141e+01	4.341e+01
3.406e+02	1.720e+00	3.271e+00	6.388e+00	3.724e+00	4.140e+01	4.352e+01
3.406e+02	1.722e+00	3.323e+00	6.492e+00	3.724e+00	4.150e+01	4.362e+01
3.407e+02	1.723e+00	3.371e+00	6.592e+00	3.725e+00	4.171e+01	4.380e+01
3.407e+02	1.725e+00	3.440e+00	6.768e+00	3.734e+00	4.210e+01	4.411e+01
3.407e+02	1.729e+00	3.487e+00	6.869e+00	3.736e+00	4.220e+01	4.428e+01
3.408e+02	1.732e+00	3.537e+00	6.990e+00	3.741e+00	4.252e+01	4.453e+01
3.928e+02	2.759e+00	3.571e+00	7.090e+00	3.749e+00	4.282e+01	4.476e+01
4.041e+02	2.837e+00	3.617e+00	7.190e+00	3.751e+00	4.291e+01	4.492e+01
4.182e+02	2.918e+00	3.663e+00	7.290e+00	3.753e+00	4.311e+01	4.502e+01
4.353e+02	3.000e+00	3.710e+00	7.390e+00	3.755e+00	4.321e+01	4.519e+01
4.566e+02	3.084e+00	3.754e+00	7.490e+00	3.757e+00	4.340e+01	4.535e+01
4.828e+02	3.169e+00	3.800e+00	7.591e+00	3.760e+00	4.350e+01	4.544e+01
5.153e+02	3.255e+00	3.846e+00	7.691e+00	3.761e+00	4.369e+01	4.561e+01
5.556e+02	3.343e+00	3.892e+00	7.791e+00	3.764e+00	4.388e+01	4.577e+01
6.054e+02	3.431e+00	3.938e+00	7.891e+00	3.765e+00	4.398e+01	4.586e+01
6.675e+02	3.521e+00	3.983e+00	7.991e+00	3.768e+00	4.417e+01	4.602e+01
7.444e+02	3.612e+00	4.027e+00	8.091e+00	3.771e+00	4.436e+01	4.618e+01
8.394e+02	3.702e+00	4.072e+00	8.191e+00	3.774e+00	4.446e+01	4.634e+01
9.581e+02	3.794e+00	4.117e+00	8.291e+00	3.776e+00	4.464e+01	4.649e+01
1.107e+03	3.887e+00	4.159e+00	8.391e+00	3.780e+00	4.482e+01	4.665e+01
1.292e+03	3.981e+00	4.201e+00	8.491e+00	3.784e+00	4.501e+01	4.685e+01
1.524e+03	4.075e+00	4.242e+00	8.591e+00	3.789e+00	4.519e+01	4.701e+01
1.813e+03	4.170e+00	4.284e+00	8.691e+00	3.793e+00	4.544e+01	4.721e+01
2.177e+03	4.265e+00	4.322e+00	8.791e+00	3.799e+00	4.562e+01	4.741e+01
2.632e+03	4.361e+00	4.361e+00	8.891e+00	3.804e+00	4.587e+01	4.761e+01
3.200e+03	4.457e+00	4.397e+00	8.991e+00	3.811e+00	4.611e+01	4.780e+01
3.912e+03	4.554e+00	4.432e+00	9.091e+00	3.819e+00	4.635e+01	4.804e+01
4.800e+03	4.650e+00	4.466e+00	9.191e+00	3.827e+00	4.665e+01	4.827e+01
5.918e+03	4.747e+00	4.494e+00	9.291e+00	3.838e+00	4.694e+01	4.853e+01
7.328e+03	4.845e+00	4.512e+00	9.391e+00	3.854e+00	4.734e+01	4.887e+01
9.081e+03	4.942e+00	4.520e+00	9.491e+00	3.875e+00	4.783e+01	4.929e+01
1.020e+04	4.994e+00	4.496e+00	9.544e+00	3.900e+00	4.832e+01	4.969e+01
1.191e+04	5.064e+00	4.482e+00	9.616e+00	3.925e+00	4.882e+01	5.006e+01
1.486e+04	5.162e+00	4.533e+00	9.716e+00	3.924e+00	4.892e+01	5.016e+01
1.855e+04	5.260e+00	4.537e+00	9.816e+00	3.947e+00	4.937e+01	5.053e+01
2.319e+04	5.359e+00	4.538e+00	9.916e+00	3.972e+00	4.980e+01	5.091e+01
2.901e+04	5.458e+00	4.543e+00	1.002e+01	3.994e+00	5.021e+01	5.124e+01

Table A1 – *continued*

3.627e+04	5.556e+00	4.556e+00	1.012e+01	4.013e+00	5.055e+01	5.151e+01
4.540e+04	5.654e+00	4.567e+00	1.022e+01	4.033e+00	5.087e+01	5.179e+01

Yorke H. W., Bodenheimer P., 2008, in Beuther H., Linz H., Henning T., eds, Astronomical Society of the Pacific Conference Series Vol. 387, Massive Star Formation: Observations Confront Theory. p. 189

This paper has been typeset from a TeX/LaTeX file prepared by the author.

Table A2. Model at $\dot{M} = 1$ M$_\odot$ yr^{-1}

age [yr]	log($M/$M$_\odot$)	log($R/$R$_\odot$)	log($L/$L$_\odot$)	log(T_{eff}[K])	log(S_{ion}[s^{-1}])	log(S_{LW}[s^{-1}])
1.000e+01	1.000e+00	2.235e+00	4.133e+00	3.678e+00	3.794e+01	4.022e+01
3.540e+02	1.270e+00	2.098e+00	3.958e+00	3.703e+00	3.840e+01	4.064e+01
3.673e+02	1.504e+00	1.965e+00	3.793e+00	3.728e+00	3.891e+01	4.099e+01
3.732e+02	1.578e+00	1.975e+00	3.894e+00	3.748e+00	3.952e+01	4.157e+01
3.732e+02	1.578e+00	1.987e+00	4.003e+00	3.769e+00	4.018e+01	4.209e+01
3.733e+02	1.579e+00	1.992e+00	4.109e+00	3.793e+00	4.086e+01	4.263e+01
3.733e+02	1.579e+00	1.996e+00	4.214e+00	3.817e+00	4.147e+01	4.311e+01
3.733e+02	1.579e+00	2.001e+00	4.318e+00	3.841e+00	4.203e+01	4.360e+01
3.733e+02	1.579e+00	2.006e+00	4.423e+00	3.865e+00	4.260e+01	4.408e+01
3.733e+02	1.580e+00	2.012e+00	4.528e+00	3.888e+00	4.312e+01	4.448e+01
3.734e+02	1.580e+00	2.019e+00	4.631e+00	3.910e+00	4.359e+01	4.488e+01
3.734e+02	1.580e+00	2.026e+00	4.734e+00	3.932e+00	4.406e+01	4.528e+01
3.734e+02	1.580e+00	2.034e+00	4.842e+00	3.955e+00	4.450e+01	4.565e+01
3.734e+02	1.581e+00	2.044e+00	4.950e+00	3.977e+00	4.490e+01	4.601e+01
3.735e+02	1.581e+00	2.055e+00	5.053e+00	3.998e+00	4.527e+01	4.629e+01
3.735e+02	1.581e+00	2.069e+00	5.156e+00	4.017e+00	4.562e+01	4.658e+01
3.735e+02	1.582e+00	2.086e+00	5.260e+00	4.034e+00	4.594e+01	4.683e+01
3.736e+02	1.582e+00	2.110e+00	5.363e+00	4.048e+00	4.620e+01	4.707e+01
3.736e+02	1.583e+00	2.142e+00	5.465e+00	4.057e+00	4.641e+01	4.725e+01
3.737e+02	1.583e+00	2.190e+00	5.566e+00	4.058e+00	4.651e+01	4.736e+01
3.737e+02	1.584e+00	2.269e+00	5.666e+00	4.044e+00	4.646e+01	4.734e+01
3.738e+02	1.585e+00	2.437e+00	5.767e+00	3.985e+00	4.584e+01	4.690e+01
3.742e+02	1.589e+00	2.954e+00	5.876e+00	3.754e+00	4.170e+01	4.367e+01
3.742e+02	1.589e+00	3.050e+00	5.989e+00	3.734e+00	4.132e+01	4.333e+01
3.743e+02	1.590e+00	3.116e+00	6.097e+00	3.728e+00	4.121e+01	4.337e+01
3.750e+02	1.598e+00	3.186e+00	6.197e+00	3.718e+00	4.110e+01	4.326e+01
4.830e+02	2.169e+00	3.214e+00	6.298e+00	3.729e+00	4.152e+01	4.357e+01
5.024e+02	2.223e+00	3.278e+00	6.398e+00	3.722e+00	4.141e+01	4.353e+01
5.267e+02	2.282e+00	3.324e+00	6.498e+00	3.724e+00	4.162e+01	4.363e+01
5.607e+02	2.353e+00	3.366e+00	6.598e+00	3.729e+00	4.183e+01	4.387e+01
6.024e+02	2.427e+00	3.409e+00	6.698e+00	3.732e+00	4.192e+01	4.404e+01
6.519e+02	2.500e+00	3.453e+00	6.798e+00	3.735e+00	4.213e+01	4.421e+01
7.105e+02	2.574e+00	3.496e+00	6.898e+00	3.739e+00	4.233e+01	4.438e+01
7.846e+02	2.653e+00	3.541e+00	6.999e+00	3.741e+00	4.253e+01	4.454e+01
8.727e+02	2.730e+00	3.586e+00	7.099e+00	3.744e+00	4.263e+01	4.464e+01
9.819e+02	2.811e+00	3.630e+00	7.199e+00	3.747e+00	4.283e+01	4.480e+01
1.117e+03	2.893e+00	3.675e+00	7.299e+00	3.749e+00	4.302e+01	4.497e+01
1.286e+03	2.978e+00	3.720e+00	7.399e+00	3.752e+00	4.312e+01	4.513e+01
1.495e+03	3.064e+00	3.766e+00	7.499e+00	3.754e+00	4.332e+01	4.529e+01
1.754e+03	3.152e+00	3.811e+00	7.599e+00	3.756e+00	4.351e+01	4.539e+01
2.075e+03	3.241e+00	3.855e+00	7.699e+00	3.759e+00	4.361e+01	4.555e+01
2.475e+03	3.330e+00	3.900e+00	7.799e+00	3.762e+00	4.380e+01	4.571e+01
2.969e+03	3.421e+00	3.945e+00	7.899e+00	3.764e+00	4.399e+01	4.587e+01
3.584e+03	3.512e+00	3.989e+00	7.999e+00	3.767e+00	4.418e+01	4.603e+01
4.350e+03	3.604e+00	4.032e+00	8.099e+00	3.771e+00	4.437e+01	4.619e+01
5.308e+03	3.697e+00	4.075e+00	8.199e+00	3.774e+00	4.446e+01	4.634e+01
6.500e+03	3.790e+00	4.117e+00	8.299e+00	3.778e+00	4.465e+01	4.650e+01
8.002e+03	3.885e+00	4.158e+00	8.399e+00	3.783e+00	4.492e+01	4.671e+01
9.863e+03	3.979e+00	4.199e+00	8.499e+00	3.787e+00	4.509e+01	4.692e+01
1.220e+04	4.074e+00	4.239e+00	8.599e+00	3.792e+00	4.527e+01	4.706e+01
1.512e+04	4.170e+00	4.278e+00	8.699e+00	3.798e+00	4.553e+01	4.727e+01
1.877e+04	4.266e+00	4.316e+00	8.799e+00	3.804e+00	4.578e+01	4.746e+01
2.336e+04	4.362e+00	4.351e+00	8.899e+00	3.811e+00	4.602e+01	4.771e+01
2.907e+04	4.458e+00	4.386e+00	8.999e+00	3.819e+00	4.626e+01	4.794e+01
3.623e+04	4.555e+00	4.418e+00	9.099e+00	3.828e+00	4.656e+01	4.817e+01
4.520e+04	4.652e+00	4.444e+00	9.199e+00	3.840e+00	4.691e+01	4.848e+01
5.644e+04	4.749e+00	4.463e+00	9.299e+00	3.855e+00	4.731e+01	4.881e+01
7.047e+04	4.846e+00	4.481e+00	9.399e+00	3.871e+00	4.768e+01	4.912e+01
8.815e+04	4.944e+00	4.493e+00	9.499e+00	3.891e+00	4.814e+01	4.952e+01
1.089e+05	5.036e+00	4.490e+00	9.593e+00	3.916e+00	4.863e+01	4.993e+01
1.363e+05	5.133e+00	4.511e+00	9.693e+00	3.930e+00	4.898e+01	5.022e+01
1.672e+05	5.222e+00	4.506e+00	9.783e+00	3.955e+00	4.944e+01	5.059e+01
2.052e+05	5.311e+00	4.501e+00	9.874e+00	3.980e+00	4.989e+01	5.095e+01

Table A3. Model at $\dot{M} = 0.1$ M$_\odot$ yr^{-1}

age [yr]	$\log(M/M_\odot)$	$\log(R/R_\odot)$	$\log(L/L_\odot)$	$\log(T_{\rm eff}[{\rm K}])$	$\log(S_{\rm ion}[{\rm s}^{-1}])$	$\log(S_{\rm LW}[{\rm s}^{-1}])$
1.000e+02	1.000e+00	2.235e+00	4.133e+00	3.678e+00	3.794e+01	4.022e+01
5.172e+02	1.260e+00	2.090e+00	3.943e+00	3.703e+00	3.838e+01	4.062e+01
5.936e+02	1.412e+00	2.112e+00	4.043e+00	3.717e+00	3.895e+01	4.103e+01
5.975e+02	1.419e+00	2.155e+00	4.144e+00	3.721e+00	3.916e+01	4.120e+01
5.982e+02	1.420e+00	2.185e+00	4.254e+00	3.733e+00	3.959e+01	4.160e+01
5.983e+02	1.420e+00	2.199e+00	4.360e+00	3.752e+00	4.018e+01	4.209e+01
5.985e+02	1.420e+00	2.210e+00	4.463e+00	3.773e+00	4.073e+01	4.261e+01
5.987e+02	1.421e+00	2.222e+00	4.567e+00	3.793e+00	4.132e+01	4.303e+01
5.990e+02	1.421e+00	2.236e+00	4.669e+00	3.811e+00	4.179e+01	4.348e+01
5.993e+02	1.422e+00	2.253e+00	4.770e+00	3.828e+00	4.223e+01	4.384e+01
5.998e+02	1.422e+00	2.273e+00	4.872e+00	3.843e+00	4.265e+01	4.419e+01
6.003e+02	1.423e+00	2.298e+00	4.974e+00	3.856e+00	4.298e+01	4.448e+01
6.011e+02	1.424e+00	2.331e+00	5.076e+00	3.865e+00	4.325e+01	4.473e+01
6.022e+02	1.426e+00	2.373e+00	5.176e+00	3.869e+00	4.346e+01	4.490e+01
6.038e+02	1.429e+00	2.431e+00	5.277e+00	3.866e+00	4.345e+01	4.493e+01
6.059e+02	1.432e+00	2.512e+00	5.378e+00	3.850e+00	4.327e+01	4.482e+01
6.086e+02	1.437e+00	2.620e+00	5.478e+00	3.822e+00	4.281e+01	4.447e+01
6.110e+02	1.440e+00	2.745e+00	5.578e+00	3.784e+00	4.209e+01	4.389e+01
6.577e+02	1.508e+00	2.941e+00	5.679e+00	3.711e+00	4.035e+01	4.259e+01
7.210e+02	1.586e+00	3.007e+00	5.790e+00	3.706e+00	4.035e+01	4.255e+01
8.122e+02	1.678e+00	3.057e+00	5.891e+00	3.706e+00	4.045e+01	4.265e+01
9.100e+02	1.759e+00	3.096e+00	5.993e+00	3.712e+00	4.078e+01	4.290e+01
1.036e+03	1.846e+00	3.153e+00	6.093e+00	3.709e+00	4.077e+01	4.293e+01
1.183e+03	1.928e+00	3.198e+00	6.193e+00	3.711e+00	4.087e+01	4.311e+01
1.356e+03	2.009e+00	3.241e+00	6.293e+00	3.715e+00	4.108e+01	4.328e+01
1.554e+03	2.086e+00	3.283e+00	6.394e+00	3.719e+00	4.129e+01	4.345e+01
1.776e+03	2.159e+00	3.326e+00	6.494e+00	3.723e+00	4.151e+01	4.363e+01
2.037e+03	2.231e+00	3.369e+00	6.594e+00	3.726e+00	4.171e+01	4.380e+01
2.354e+03	2.305e+00	3.415e+00	6.694e+00	3.728e+00	4.181e+01	4.397e+01
2.753e+03	2.383e+00	3.460e+00	6.794e+00	3.731e+00	4.202e+01	4.407e+01
3.258e+03	2.466e+00	3.504e+00	6.894e+00	3.734e+00	4.222e+01	4.423e+01
3.886e+03	2.550e+00	3.549e+00	6.994e+00	3.736e+00	4.232e+01	4.440e+01
4.658e+03	2.636e+00	3.595e+00	7.094e+00	3.738e+00	4.253e+01	4.457e+01
5.624e+03	2.723e+00	3.640e+00	7.194e+00	3.740e+00	4.273e+01	4.467e+01
6.828e+03	2.812e+00	3.685e+00	7.294e+00	3.743e+00	4.282e+01	4.484e+01
8.331e+03	2.903e+00	3.729e+00	7.395e+00	3.746e+00	4.302e+01	4.500e+01
1.021e+04	2.995e+00	3.775e+00	7.495e+00	3.748e+00	4.312e+01	4.517e+01
1.235e+04	3.080e+00	3.826e+00	7.601e+00	3.749e+00	4.333e+01	4.527e+01
1.568e+04	3.186e+00	3.863e+00	7.701e+00	3.756e+00	4.352e+01	4.550e+01
1.940e+04	3.280e+00	3.911e+00	7.802e+00	3.757e+00	4.371e+01	4.559e+01
2.406e+04	3.375e+00	3.956e+00	7.902e+00	3.760e+00	4.381e+01	4.576e+01
2.986e+04	3.470e+00	3.998e+00	8.002e+00	3.763e+00	4.400e+01	4.598e+01
3.716e+04	3.566e+00	4.041e+00	8.102e+00	3.767e+00	4.419e+01	4.613e+01
4.632e+04	3.663e+00	4.084e+00	8.202e+00	3.771e+00	4.438e+01	4.629e+01
5.778e+04	3.759e+00	4.125e+00	8.302e+00	3.775e+00	4.465e+01	4.644e+01
7.218e+04	3.856e+00	4.167e+00	8.402e+00	3.779e+00	4.484e+01	4.666e+01
9.023e+04	3.954e+00	4.207e+00	8.502e+00	3.784e+00	4.502e+01	4.681e+01
1.129e+05	4.051e+00	4.247e+00	8.602e+00	3.789e+00	4.520e+01	4.702e+01
1.413e+05	4.149e+00	4.287e+00	8.702e+00	3.794e+00	4.545e+01	4.722e+01
1.770e+05	4.247e+00	4.325e+00	8.802e+00	3.800e+00	4.571e+01	4.742e+01
2.219e+05	4.345e+00	4.362e+00	8.902e+00	3.807e+00	4.595e+01	4.761e+01
2.782e+05	4.444e+00	4.398e+00	9.002e+00	3.814e+00	4.619e+01	4.785e+01
3.490e+05	4.542e+00	4.429e+00	9.102e+00	3.823e+00	4.650e+01	4.809e+01
4.381e+05	4.641e+00	4.453e+00	9.202e+00	3.836e+00	4.686e+01	4.840e+01
5.498e+05	4.740e+00	4.469e+00	9.302e+00	3.853e+00	4.725e+01	4.878e+01
6.713e+05	4.827e+00	4.462e+00	9.388e+00	3.878e+00	4.783e+01	4.921e+01

Table A4. Model at $\dot{M} = 0.01$ M$_\odot$ yr^{-1}

age [yr]	log(M/M$_\odot$)	log(R/R$_\odot$)	log(L/L$_\odot$)	log($T_{\rm eff}$[K])	log($S_{\rm ion}$[s^{-1}])	log($S_{\rm LW}$[s^{-1}])
2.100e+02	3.222e-01	1.381e+00	2.499e+00	3.696e+00	3.682e+01	3.901e+01
4.030e+02	6.053e-01	1.285e+00	2.408e+00	3.722e+00	3.742e+01	3.954e+01
7.284e+02	8.623e-01	1.193e+00	2.325e+00	3.747e+00	3.795e+01	3.993e+01
1.173e+03	1.069e+00	1.197e+00	2.425e+00	3.770e+00	3.860e+01	4.052e+01
1.192e+03	1.076e+00	1.240e+00	2.562e+00	3.782e+00	3.908e+01	4.087e+01
1.192e+03	1.076e+00	1.248e+00	2.679e+00	3.808e+00	3.973e+01	4.144e+01
1.192e+03	1.076e+00	1.256e+00	2.788e+00	3.831e+00	4.031e+01	4.190e+01
1.193e+03	1.077e+00	1.260e+00	2.893e+00	3.855e+00	4.090e+01	4.240e+01
1.193e+03	1.077e+00	1.261e+00	2.999e+00	3.881e+00	4.149e+01	4.289e+01
1.193e+03	1.077e+00	1.248e+00	3.085e+00	3.909e+00	4.204e+01	4.334e+01
1.193e+03	1.077e+00	1.273e+00	3.195e+00	3.924e+00	4.240e+01	4.364e+01
1.194e+03	1.077e+00	1.277e+00	3.307e+00	3.950e+00	4.289e+01	4.404e+01
1.194e+03	1.077e+00	1.281e+00	3.407e+00	3.973e+00	4.333e+01	4.440e+01
1.194e+03	1.077e+00	1.288e+00	3.508e+00	3.995e+00	4.370e+01	4.473e+01
1.195e+03	1.077e+00	1.292e+00	3.615e+00	4.020e+00	4.413e+01	4.507e+01
1.195e+03	1.077e+00	1.296e+00	3.718e+00	4.043e+00	4.451e+01	4.538e+01
1.196e+03	1.078e+00	1.301e+00	3.819e+00	4.066e+00	4.484e+01	4.568e+01
1.196e+03	1.078e+00	1.310e+00	3.938e+00	4.091e+00	4.522e+01	4.599e+01
1.197e+03	1.078e+00	1.319e+00	4.041e+00	4.113e+00	4.554e+01	4.624e+01
1.198e+03	1.079e+00	1.330e+00	4.144e+00	4.133e+00	4.582e+01	4.647e+01
1.200e+03	1.079e+00	1.346e+00	4.248e+00	4.151e+00	4.608e+01	4.668e+01
1.202e+03	1.080e+00	1.362e+00	4.352e+00	4.169e+00	4.633e+01	4.689e+01
1.206e+03	1.081e+00	1.384e+00	4.453e+00	4.183e+00	4.653e+01	4.706e+01
1.212e+03	1.084e+00	1.412e+00	4.559e+00	4.196e+00	4.673e+01	4.723e+01
1.223e+03	1.088e+00	1.452e+00	4.659e+00	4.201e+00	4.687e+01	4.736e+01
1.240e+03	1.094e+00	1.497e+00	4.761e+00	4.204e+00	4.699e+01	4.747e+01
1.269e+03	1.103e+00	1.561e+00	4.861e+00	4.197e+00	4.704e+01	4.754e+01
1.316e+03	1.119e+00	1.643e+00	4.962e+00	4.181e+00	4.703e+01	4.756e+01
1.392e+03	1.144e+00	1.743e+00	5.062e+00	4.156e+00	4.693e+01	4.753e+01
1.512e+03	1.180e+00	1.850e+00	5.162e+00	4.128e+00	4.679e+01	4.745e+01
1.700e+03	1.231e+00	1.933e+00	5.262e+00	4.111e+00	4.674e+01	4.745e+01
1.965e+03	1.293e+00	1.963e+00	5.362e+00	4.121e+00	4.693e+01	4.761e+01
2.210e+03	1.344e+00	1.950e+00	5.436e+00	4.146e+00	4.722e+01	4.784e+01
2.419e+03	1.384e+00	1.928e+00	5.493e+00	4.171e+00	4.748e+01	4.804e+01
2.624e+03	1.419e+00	1.904e+00	5.544e+00	4.196e+00	4.772e+01	4.822e+01
2.833e+03	1.452e+00	1.878e+00	5.593e+00	4.221e+00	4.794e+01	4.839e+01
3.054e+03	1.485e+00	1.852e+00	5.642e+00	4.246e+00	4.815e+01	4.854e+01
3.292e+03	1.517e+00	1.827e+00	5.691e+00	4.271e+00	4.835e+01	4.869e+01
3.548e+03	1.550e+00	1.802e+00	5.741e+00	4.296e+00	4.853e+01	4.882e+01
3.833e+03	1.584e+00	1.778e+00	5.793e+00	4.321e+00	4.871e+01	4.894e+01
4.152e+03	1.618e+00	1.755e+00	5.848e+00	4.346e+00	4.888e+01	4.906e+01
4.525e+03	1.656e+00	1.735e+00	5.906e+00	4.371e+00	4.904e+01	4.917e+01
4.980e+03	1.697e+00	1.718e+00	5.972e+00	4.396e+00	4.920e+01	4.929e+01
5.609e+03	1.749e+00	1.708e+00	6.054e+00	4.421e+00	4.937e+01	4.941e+01
6.495e+03	1.813e+00	1.722e+00	6.154e+00	4.439e+00	4.953e+01	4.954e+01
7.541e+03	1.877e+00	1.779e+00	6.254e+00	4.436e+00	4.962e+01	4.963e+01
8.809e+03	1.945e+00	1.905e+00	6.355e+00	4.398e+00	4.959e+01	4.967e+01
1.048e+04	2.020e+00	2.105e+00	6.455e+00	4.323e+00	4.938e+01	4.961e+01
1.279e+04	2.107e+00	2.214e+00	6.555e+00	4.293e+00	4.933e+01	4.962e+01
1.392e+04	2.144e+00	2.184e+00	6.594e+00	4.318e+00	4.950e+01	4.974e+01
1.470e+04	2.167e+00	2.146e+00	6.618e+00	4.344e+00	4.964e+01	4.982e+01
1.534e+04	2.186e+00	2.105e+00	6.637e+00	4.369e+00	4.976e+01	4.990e+01
1.596e+04	2.203e+00	2.064e+00	6.655e+00	4.394e+00	4.988e+01	4.997e+01
1.659e+04	2.220e+00	2.022e+00	6.671e+00	4.419e+00	4.998e+01	5.002e+01
1.735e+04	2.239e+00	1.983e+00	6.694e+00	4.444e+00	5.008e+01	5.008e+01
1.812e+04	2.258e+00	1.943e+00	6.714e+00	4.469e+00	5.017e+01	5.013e+01
1.895e+04	2.278e+00	1.903e+00	6.735e+00	4.494e+00	5.026e+01	5.017e+01
2.013e+04	2.304e+00	1.868e+00	6.765e+00	4.519e+00	5.034e+01	5.021e+01
2.182e+04	2.339e+00	1.839e+00	6.806e+00	4.544e+00	5.044e+01	5.025e+01
2.619e+04	2.418e+00	1.949e+00	6.906e+00	4.514e+00	5.048e+01	5.034e+01
3.151e+04	2.499e+00	2.622e+00	7.006e+00	4.203e+00	4.922e+01	4.971e+01
3.527e+04	2.547e+00	2.596e+00	7.055e+00	4.228e+00	4.944e+01	4.988e+01
3.583e+04	2.554e+00	2.549e+00	7.061e+00	4.253e+00	4.961e+01	4.999e+01

Table A4 – *continued*

3.639e+04	2.561e+00	2.502e+00	7.068e+00	4.278e+00	4.976e+01	5.008e+01
3.694e+04	2.567e+00	2.455e+00	7.074e+00	4.303e+00	4.990e+01	5.017e+01
3.753e+04	2.574e+00	2.408e+00	7.080e+00	4.328e+00	5.003e+01	5.025e+01
3.818e+04	2.582e+00	2.362e+00	7.087e+00	4.353e+00	5.014e+01	5.032e+01
3.884e+04	2.589e+00	2.315e+00	7.095e+00	4.378e+00	5.025e+01	5.038e+01
3.958e+04	2.597e+00	2.269e+00	7.103e+00	4.403e+00	5.035e+01	5.043e+01
4.038e+04	2.606e+00	2.224e+00	7.111e+00	4.428e+00	5.045e+01	5.048e+01
4.127e+04	2.616e+00	2.178e+00	7.121e+00	4.453e+00	5.053e+01	5.052e+01
4.229e+04	2.626e+00	2.134e+00	7.131e+00	4.478e+00	5.061e+01	5.055e+01
4.341e+04	2.638e+00	2.089e+00	7.143e+00	4.503e+00	5.069e+01	5.058e+01
4.480e+04	2.651e+00	2.046e+00	7.157e+00	4.528e+00	5.076e+01	5.060e+01
4.665e+04	2.669e+00	2.006e+00	7.176e+00	4.553e+00	5.082e+01	5.062e+01
5.608e+04	2.749e+00	2.406e+00	7.276e+00	4.378e+00	5.044e+01	5.056e+01
6.911e+04	2.840e+00	3.702e+00	7.376e+00	3.755e+00	4.319e+01	4.517e+01
8.395e+04	2.924e+00	3.753e+00	7.476e+00	3.754e+00	4.330e+01	4.527e+01
1.056e+05	3.024e+00	3.778e+00	7.579e+00	3.768e+00	4.376e+01	4.561e+01
1.381e+05	3.140e+00	3.848e+00	7.679e+00	3.758e+00	4.359e+01	4.553e+01
1.458e+05	3.164e+00	3.803e+00	7.699e+00	3.785e+00	4.421e+01	4.606e+01
1.695e+05	3.229e+00	3.907e+00	7.799e+00	3.758e+00	4.371e+01	4.565e+01
2.232e+05	3.349e+00	3.948e+00	7.899e+00	3.763e+00	4.390e+01	4.581e+01
2.777e+05	3.444e+00	3.987e+00	7.999e+00	3.768e+00	4.418e+01	4.603e+01
3.505e+05	3.545e+00	4.032e+00	8.099e+00	3.771e+00	4.428e+01	4.619e+01
4.413e+05	3.645e+00	4.071e+00	8.199e+00	3.776e+00	4.455e+01	4.640e+01
5.442e+05	3.736e+00	4.087e+00	8.299e+00	3.793e+00	4.505e+01	4.682e+01
6.905e+05	3.839e+00	4.149e+00	8.399e+00	3.787e+00	4.499e+01	4.682e+01
8.634e+05	3.936e+00	4.185e+00	8.499e+00	3.794e+00	4.525e+01	4.702e+01
1.084e+06	4.035e+00	4.223e+00	8.599e+00	3.800e+00	4.550e+01	4.721e+01
1.361e+06	4.134e+00	4.255e+00	8.699e+00	3.809e+00	4.575e+01	4.746e+01

Table A5. Model at $\dot{M} = 0.001$ M$_\odot$ yr^{-1}

age [yr]	log(M/M$_\odot$)	log(R/R$_\odot$)	log(L/L$_\odot$)	log($T_{\rm eff}$[K])	log($S_{\rm ion}$[s^{-1}])	log($S_{\rm LW}$[s^{-1}])
2.010e+03	3.032e-01	1.368e+00	2.474e+00	3.696e+00	3.679e+01	3.899e+01
3.672e+03	5.649e-01	1.239e+00	2.316e+00	3.721e+00	3.733e+01	3.945e+01
6.607e+03	8.200e-01	1.186e+00	2.309e+00	3.746e+00	3.794e+01	3.991e+01
7.180e+03	8.561e-01	1.227e+00	2.410e+00	3.751e+00	3.813e+01	4.014e+01
7.323e+03	8.647e-01	1.270e+00	2.513e+00	3.755e+00	3.833e+01	4.031e+01
7.340e+03	8.657e-01	1.311e+00	2.635e+00	3.765e+00	3.873e+01	4.061e+01
7.348e+03	8.662e-01	1.343e+00	2.752e+00	3.778e+00	3.919e+01	4.101e+01
7.357e+03	8.667e-01	1.356e+00	2.853e+00	3.797e+00	3.968e+01	4.142e+01
7.369e+03	8.674e-01	1.368e+00	2.966e+00	3.820e+00	4.030e+01	4.191e+01
7.384e+03	8.683e-01	1.380e+00	3.073e+00	3.840e+00	4.079e+01	4.235e+01
7.405e+03	8.695e-01	1.393e+00	3.181e+00	3.861e+00	4.130e+01	4.276e+01
7.436e+03	8.713e-01	1.408e+00	3.290e+00	3.881e+00	4.173e+01	4.315e+01
7.479e+03	8.738e-01	1.424e+00	3.393e+00	3.899e+00	4.217e+01	4.350e+01
7.546e+03	8.777e-01	1.442e+00	3.496e+00	3.915e+00	4.254e+01	4.384e+01
7.657e+03	8.841e-01	1.462e+00	3.602e+00	3.932e+00	4.289e+01	4.412e+01
7.828e+03	8.937e-01	1.481e+00	3.703e+00	3.947e+00	4.325e+01	4.442e+01
8.097e+03	9.083e-01	1.497e+00	3.805e+00	3.965e+00	4.360e+01	4.472e+01
8.493e+03	9.291e-01	1.503e+00	3.905e+00	3.987e+00	4.398e+01	4.503e+01
8.972e+03	9.529e-01	1.498e+00	3.995e+00	4.012e+00	4.440e+01	4.539e+01
9.458e+03	9.758e-01	1.484e+00	4.068e+00	4.037e+00	4.477e+01	4.569e+01
9.939e+03	9.973e-01	1.466e+00	4.133e+00	4.062e+00	4.512e+01	4.595e+01
1.043e+04	1.018e+00	1.446e+00	4.192e+00	4.087e+00	4.544e+01	4.621e+01
1.092e+04	1.038e+00	1.424e+00	4.248e+00	4.112e+00	4.573e+01	4.645e+01
1.143e+04	1.058e+00	1.400e+00	4.302e+00	4.137e+00	4.602e+01	4.665e+01
1.194e+04	1.077e+00	1.376e+00	4.355e+00	4.163e+00	4.627e+01	4.685e+01
1.247e+04	1.096e+00	1.351e+00	4.406e+00	4.188e+00	4.652e+01	4.705e+01
1.302e+04	1.114e+00	1.325e+00	4.455e+00	4.213e+00	4.675e+01	4.721e+01
1.357e+04	1.132e+00	1.299e+00	4.503e+00	4.238e+00	4.697e+01	4.737e+01
1.414e+04	1.150e+00	1.272e+00	4.551e+00	4.264e+00	4.717e+01	4.752e+01
1.473e+04	1.168e+00	1.244e+00	4.597e+00	4.289e+00	4.735e+01	4.765e+01
1.534e+04	1.186e+00	1.217e+00	4.642e+00	4.314e+00	4.752e+01	4.777e+01
1.596e+04	1.203e+00	1.189e+00	4.686e+00	4.339e+00	4.768e+01	4.789e+01
1.662e+04	1.221e+00	1.160e+00	4.730e+00	4.365e+00	4.783e+01	4.799e+01
1.731e+04	1.238e+00	1.131e+00	4.774e+00	4.390e+00	4.798e+01	4.808e+01
1.803e+04	1.256e+00	1.102e+00	4.818e+00	4.416e+00	4.811e+01	4.817e+01
1.878e+04	1.274e+00	1.073e+00	4.861e+00	4.441e+00	4.824e+01	4.824e+01
1.956e+04	1.291e+00	1.043e+00	4.904e+00	4.466e+00	4.836e+01	4.831e+01
2.036e+04	1.309e+00	1.014e+00	4.947e+00	4.492e+00	4.846e+01	4.837e+01
2.121e+04	1.327e+00	9.848e-01	4.989e+00	4.517e+00	4.856e+01	4.843e+01
2.212e+04	1.345e+00	9.548e-01	5.030e+00	4.542e+00	4.866e+01	4.847e+01
2.307e+04	1.363e+00	9.244e-01	5.072e+00	4.568e+00	4.875e+01	4.852e+01
2.407e+04	1.381e+00	8.949e-01	5.113e+00	4.593e+00	4.883e+01	4.856e+01
2.512e+04	1.400e+00	8.653e-01	5.154e+00	4.618e+00	4.890e+01	4.859e+01
2.622e+04	1.419e+00	8.358e-01	5.196e+00	4.643e+00	4.898e+01	4.862e+01
2.738e+04	1.437e+00	8.068e-01	5.239e+00	4.668e+00	4.905e+01	4.864e+01
2.860e+04	1.456e+00	7.781e-01	5.282e+00	4.694e+00	4.911e+01	4.867e+01
2.988e+04	1.475e+00	7.504e-01	5.328e+00	4.719e+00	4.918e+01	4.869e+01
3.120e+04	1.494e+00	7.232e-01	5.375e+00	4.744e+00	4.924e+01	4.870e+01
3.258e+04	1.513e+00	6.960e-01	5.420e+00	4.769e+00	4.929e+01	4.872e+01
3.403e+04	1.532e+00	6.686e-01	5.466e+00	4.794e+00	4.935e+01	4.873e+01
3.557e+04	1.551e+00	6.411e-01	5.511e+00	4.819e+00	4.940e+01	4.874e+01
3.721e+04	1.571e+00	6.138e-01	5.557e+00	4.844e+00	4.945e+01	4.874e+01
3.899e+04	1.591e+00	5.866e-01	5.603e+00	4.870e+00	4.949e+01	4.874e+01
4.094e+04	1.612e+00	5.591e-01	5.649e+00	4.895e+00	4.954e+01	4.875e+01
4.543e+04	1.657e+00	5.374e-01	5.705e+00	4.920e+00	4.959e+01	4.876e+01
5.472e+04	1.738e+00	5.057e-01	5.742e+00	4.945e+00	4.962e+01	4.874e+01
6.636e+04	1.822e+00	5.357e-01	5.842e+00	4.955e+00	4.972e+01	4.883e+01
7.631e+04	1.883e+00	5.691e-01	5.942e+00	4.963e+00	4.982e+01	4.891e+01
8.784e+04	1.944e+00	6.047e-01	6.042e+00	4.970e+00	4.991e+01	4.899e+01
1.014e+05	2.006e+00	6.414e-01	6.142e+00	4.977e+00	5.001e+01	4.908e+01
1.173e+05	2.069e+00	6.798e-01	6.243e+00	4.983e+00	5.011e+01	4.917e+01
1.363e+05	2.135e+00	7.194e-01	6.343e+00	4.988e+00	5.021e+01	4.926e+01
1.591e+05	2.202e+00	7.600e-01	6.443e+00	4.993e+00	5.031e+01	4.935e+01

Table A5 – *continued*

1.864e+05	2.270e+00	8.003e-01	6.543e+00	4.998e+00	5.041e+01	4.944e+01
2.194e+05	2.341e+00	8.408e-01	6.643e+00	5.002e+00	5.050e+01	4.953e+01
2.596e+05	2.414e+00	8.827e-01	6.743e+00	5.006e+00	5.060e+01	4.962e+01
3.083e+05	2.489e+00	9.281e-01	6.843e+00	5.009e+00	5.070e+01	4.971e+01
3.678e+05	2.566e+00	9.758e-01	6.943e+00	5.010e+00	5.080e+01	4.981e+01
4.403e+05	2.644e+00	1.023e+00	7.043e+00	5.011e+00	5.090e+01	4.991e+01
5.289e+05	2.723e+00	1.075e+00	7.143e+00	5.010e+00	5.100e+01	5.001e+01
6.373e+05	2.804e+00	1.128e+00	7.243e+00	5.009e+00	5.110e+01	5.011e+01
7.688e+05	2.886e+00	1.186e+00	7.343e+00	5.005e+00	5.120e+01	5.022e+01
9.324e+05	2.970e+00	1.247e+00	7.443e+00	4.999e+00	5.131e+01	5.033e+01
1.137e+06	3.056e+00	1.309e+00	7.543e+00	4.993e+00	5.141e+01	5.045e+01
1.388e+06	3.142e+00	1.382e+00	7.643e+00	4.982e+00	5.151e+01	5.057e+01
1.714e+06	3.234e+00	1.446e+00	7.743e+00	4.975e+00	5.161e+01	5.069e+01
2.111e+06	3.325e+00	1.513e+00	7.844e+00	4.966e+00	5.172e+01	5.080e+01
2.609e+06	3.416e+00	1.585e+00	7.944e+00	4.955e+00	5.182e+01	5.092e+01
3.228e+06	3.509e+00	1.676e+00	8.044e+00	4.935e+00	5.193e+01	5.107e+01
4.011e+06	3.603e+00	1.769e+00	8.144e+00	4.913e+00	5.203e+01	5.121e+01
4.989e+06	3.698e+00	1.870e+00	8.244e+00	4.888e+00	5.213e+01	5.135e+01
6.220e+06	3.794e+00	1.936e+00	8.344e+00	4.880e+00	5.223e+01	5.147e+01
7.756e+06	3.890e+00	2.092e+00	8.444e+00	4.827e+00	5.233e+01	5.166e+01
8.579e+06	3.933e+00	2.065e+00	8.489e+00	4.852e+00	5.238e+01	5.166e+01
1.073e+07	4.030e+00	2.281e+00	8.589e+00	4.769e+00	5.246e+01	5.189e+01
1.164e+07	4.066e+00	2.278e+00	8.684e+00	4.794e+00	5.257e+01	5.195e+01